PAPER

Check for updates

Scalable and bright: unlocking functional silicon quantum dots with near-unity internal quantum yield through universal plasma-driven engineering

Filip Matějka, [ID] *[a,b] Pavel Galář, [ID] [a] Josef Khun,[b] Milan Dopita,[c] Alena Michalcová, [ID] [b] Tomáš Popelář, [ID] [a] Jan Benedikt [ID] [d] and Kateřina Kůsová [ID] [a]

Silicon quantum dots (SiQDs) are a promising class of functional nanomaterials combining non-toxicity, in comparison with their binary counterparts, and tunable optoelectronic properties. However, reaching their full potential in applications requires scalable fabrication and fast and simpler modification methods, enabling bonding of a broad variety of ligands and control over the photoluminescence efficiency. Here, we advance a versatile synthesis–modification methodology based on non-thermal plasma. In particular, we complement synthesis in non-thermal plasma allowing for extensive size tuning of SiQDs with unconventional air-free plasma-induced in-liquid reactions (PILRs) which enable rapid attachment of diverse ligands, using 3D-printed components for atmospheric control. Our approach yields brightly luminescent SiQDs with diameters starting from 2.4 nm with quantum yields of up to 20% and excellent colloidal stability across solvents of varying polarity. Spectrally resolved lifetime analysis uncovers a near-unity internal quantum yield for bright SiQDs and reveals how surface chemistry and aggregation govern dark-to-bright QD population ratios and photoluminescence quenching. Additionally, we simplify the well-established protocols of thermal hydrosilylation, showing that controlled-atmosphere sample collection without any further purification steps is a necessary condition for obtaining monodispersions with good optical properties. These results define a simple route to functionally engineered SiQDs, providing new insight into emission dynamics and establishing a strong foundation for their integration into advanced photonic, bioimaging, and energy-harvesting devices.

1. Introduction

Silicon quantum dots (SiQDs) have gained significant interest due to their optoelectronic properties and chemical versatility.[1–3] Silicon's natural abundance, biocompatibility, and environmentally friendly form make it attractive for a wide variety of applications ranging from solar cells and solar concentrators[4–6] to light-emitting diodes and sensors,[7–10] bioimaging,[11] theranostics[12] and batteries.[13,14]

The most common approaches for the synthesis of photoluminescence (PL)-emitting SiQDs are: (i) low-[15–17] or atmospheric-pressure[18,19] plasma synthesis from the gaseous (*e.g.* silane) or even liquid precursors, (cyclohexasilane[20]) and (ii)

the thermal disproportionation of silicon-rich silicon oxide such as hydrogen silsesquioxane[21] (HSQ), triethoxysilane[22] or in layered plasma-deposited superlattices.[23] Both the methods are capable of producing SiQDs with a relatively narrow (±30%) size distribution. Other synthesis methods include solution synthesis from *e.g.* halide salts or alkali silicides,[24] some of which have been recently critiqued due to the potential production of light-emitting carbon QDs.[25–27] Surprisingly, SiQDs can even be synthesized from rice husks.[10]

The advantage of the disproportionation approach is the low initial cost of the precursor material and good control over the size of the resulting SiQDs. Its main drawback is a combination of energy-extensive (*e.g.* high temperature annealing at 1100 °C) and time-consuming (*e.g.* grinding) steps and the use of dangerous chemicals (hydrofluoric acid, silanes formed during the annealing steps[21,28]). In contrast to that, low-pressure non-thermal plasma synthesis (LP-NTP) is faster with fewer steps and lower energy consumption, even though it requires rather expensive vacuum equipment. The precursor mixture of 1% silane in argon is not flammable and can be bought pre-mixed in a cylinder.[17,29] The good control over the size and structure of the resulting SiQDs can be achieved by

[a]Institute of Physics of the CAS, v.v.i., Cukrovarnická 10, 162 00 Prague 6, Czechia. E-mail: matejkaf@fzu.cz
[b]Faculty of Chemical Engineering, University of Chemistry and Technology, Technická 5, 166 28 Praha 6, Czechia
[c]Faculty of Mathematics and Physics, Charles University, Ke Karlovu 3, 121 16 Praha 2, Czechia
[d]Institute of Experimental and Applied Physics, Kiel University, Leibnizstraße 19, 24118 Kiel, Germany

adjusting the precursor flow, residence time (time spent in the plasma discharge) and plasma geometry.[30] Both plasma synthesis and thermal disproportionation lead to hydrogen-terminated surfaces (SiH_x, $x = 1$, 2, and 3), even though they can potentially lead to structurally different surfaces with different surface reactivities.[31] Hydrogen-terminated H:SiQDs are strongly prone to oxidative processes when exposed to atmospheric oxygen and water vapor. Thus, strict control of air exposure is required if other than oxide-based termination is sought.

The state-of-the-art surface modification is hydrosilylation using long-chain alkyls.[2,32] The original thermal hydrosilylation method, based on the homolytic cleavage of Si–H occurring at ≈150 °C, limits the ligand choices only to high temperature boiling liquids.[33,34] As an alternative, a radically initiated (using e.g. 2,2′-azobis(2-methylpropionitrile) (AIBN) or 1,1′-azobis(cyclohexanecarbonitrile) (ABCN)),[35,36] photoinitiated,[37] or microwave assisted hydrosilylation reaction[38] can be employed. Interestingly, even room-temperature hydrosilylation was introduced for specific molecules (e.g. styrene).[39] The disadvantages of these processes include the usage of expensive and persistent catalysts, expensive mediator chemicals, the potential size dependent reactivity[35–37] and a long reaction time, ranging from several hours to days.[40] Due to the sensitivity of the reactants to atmospheric oxygen and humidity, the hydrosilylation process is typically carried out under an inert atmosphere (commonly in glove boxes) and several freeze–pump–thaw cycles of the solvents using the Schlenk line are necessary.[35] Therefore, there is still room for improvement if these methods were to be broadly used.

An important aspect of the modification process is the need to expand the variety of termination molecules to achieve dispersions of SiQDs in environments of different polarities, from highly polar such as water and ethanol to non-polar such as toluene. As of now, water-based dispersions achieved through polar terminal groups are problematic despite their importance for bioapplications.[11,41,42] Here, a possible alternative to the hydrosilylation process is the employment of non-thermal plasma (NTP) discharge to initiate the plasma-induced in-liquid reactions (PILRs). The discharge provides a highly reactive and reactant-dense medium, leading to fast kinetics of the initiated chemical reactions while keeping the process temperature low. Moreover, NTP can provide a wider range of ligands because the need for the terminal double bond in a hydrosilylation process is replaced with the generation of highly energetic electrons that can dissociate weaker bonds.[43,44] The NTP-based surface modification is also tunable by experimental geometry, employing a spark, a jet, or a corona discharge in the gas phase[43] or point-to-plane microplasma[45,46] in a liquid-to-gas interface. The PILR method is also easily up-scalable, e.g. by deploying parallelly connected reactors. Recently, the point-to-plane microplasma geometry was used to enrich oxidized SiQDs with nitrogen-based species using only air and water as the source of chemicals[47] with a fast reaction time from 30 to 40 minutes if the geometry of the experiment was optimized to restrict the air flow to the reac-

tion vessel.[48] The potential of the PILR is supported by other published pioneering works, which focused on reactions induced in a water environment and attachment of short alkyl molecules (e.g. ethanol) using a mixture of the alkyl liquid and water for the plasma initiated reactions,[42,45,49] or on the preparation of oxidized water dispersible SiQDs with photoluminescence quantum yields (QY) reaching 50% using a mixture of ethanol and water and an argon plasma jet.[42] As PILR does not proceed in a completely water- and oxygen-free environment, the expected modification outcome if organic groups are used as the prospective ligand is alkoxylation combined with a degree of oxidation of the surface. Even if alternative approaches to alkoxylation exist,[50–52] PILR represents a promising alternative or extension to hydrosilylation, broadening the variety of terminating groups, offering up-scalability and significantly decreased reaction times.

Apart from preventing the uncontrolled oxidation process and tuning the dispersibility in different polar environments, modification techniques are commonly employed to impart stability and enhance PL properties. Even though more PL channels exist,[53–56] PL is typically represented by a broad PL band tunable between the red visible spectral region and the near infrared region (size ranging from ca. 2 to 7 nm), with photoluminescence QYs often close to 5%, but sometimes reaching[22,36,57,58] 20% or even 60%.[59] Also, as has been shown recently,[60] due to long radiative lifetimes of this PL channel, dark QDs are often responsible for the lower QYs, while the quenching mechanism in dark SiQDs still remains uncertain.

Therefore, finding a trade-off between dispersibility in environments with different polarities, tunability of sizes, stability and emission properties using a fast, technically non-demanding and up-scalable process is still a substantial and challenging task. In this regard, this article represents a comprehensive overview of the LP-NTP synthesis and basic modification procedures in SiQDs. In addition to a detailed discussion of the standard fabrication and characterization methods, we put emphasis on simplifying the modification and reaching good dispersability in environments with a broad range of polarities. Specifically, using our synthesis protocols, we were able to tune the sizes of the produced SiQDs in a broad range (2.4–6 nm) predominantly by increasing the hydrogen flow in the synthesis gas mixture. Moreover, we showed that it is possible to reach excellent dispersibility, a low degree of oligomerization of surface ligands and good optical performance in comparison with typical samples utilizing basic thermal hydrosilylation. In particular, PL quantum yields reach 20% and lifetimes of the emitting QDs are fully radiative. We used a simple collect-and-cook approach, where the collection in a protective atmosphere and heating in argon-filled closed containers were the only protective and purification steps necessary in the procedure. Additionally, we introduced a modification method based on pulsed NTP-microplasma-initiated reactions (PILRs). The PILR-based air-free surface modification offered much shorter reaction times than hydrosilation (45 minutes vs. tens of hours). It also removed the requirement for the terminal double bond in the ligand to be attached,

leading to mostly alkoxylated surfaces and dispersibilities in more polar environments. Last but not least, we applied a dedicated optical characterization method that we recently introduced,[60] which confirmed a similar PL dynamics in hydrosilylated, carbon-linked and PILR-produced alkoxylated samples. This similarity in PL dynamics underscores the importance of identifying the mechanisms behind dark QDs which then determine the overall PL performance. Our quantification of the fraction of dark SiQDs allowed us to identify aggregation as one factor contributing to PL quenching through dark SiQDs.

This paper is structured as follows. Section 2 contains the details of the applied methods. Section 3.1 describes the synthesis and PILR surface modification. Section 3.2 introduces our approach to thermal hydrosilylation. The two following sections, sections 3.3 and 3.4, are devoted to the structural, chemical and optical characterization of the fabricated SiQDs. The paper closes with conclusions in section 4.

2. Experimental

2.1. Used chemicals and gases

Synthesis gases: argon (*Linde*, Ar 6.0), diluted silane (*Linde*, 1% in argon, Ar 5.7, SiH_4 5.0) and hydrogen (*Linde*, H_2 7.0). Gases in Synth-box and PILR-Box: argon (*Linde*, Ar 4.7) and nitrogen (central institutional distribution, N_2 5.0). Used chemicals are: 1-dodecene (Sigma-Aldrich, 95%); octan-1-ol (Penta, p.a.); ethanol (Penta, absolute for UV); acetic acid (Penta, 99%), phenol (Sigma-Aldrich, 99%), toluene (Sigma-Aldrich, HPLC Plus and residue analysis, ≥99.9%); propan-2-ol (Penta, isopropyl acohol for UV, ≥99.5%); acetonitrile (Sigma-Aldrich, suitable for HPLC, ≥99.9%), and hydrofluoric acid (Penta, 50%, p.a.). All non-polar reactants were stored over molecular sieves (4Å, beads, Sigma-Aldrich).

2.2. Synthesis of H:SiQDs from silane gas

SiQDs were synthesized in a noncommercial flow-through reactor with low-pressure non-thermal plasma. The reactor was made up of a one-meter-long glass tube with an inner diameter of 0.8 cm, attached with copper planar electrodes (dimensions: 5 cm by 12 cm). The electrodes were placed parallel to the glass tube with the distance slightly exceeding 10 mm so they almost touched the glass tube walls. One of the electrodes was grounded while the other one was powered by the RF generator. In this glass tube reactor, capacitively coupled plasma was generated using an RF power source RFG-600W from Coaxial Power Systems operating at the frequency of 13.56 MHz, coupled to the high efficiency automatic matching network AMN-600 (Coaxial Power Systems). The output source power was set to 150 W. The system was operated under low pressure; thus, the tubing after the sample collector was vacuum ready and the setup was pumped by the fore vacuum pump (the pressure in standby is within 10 Pa, in the synthesis mode, the pressure was lower than 500 Pa). Synthesis gases were argon as the carrier gas, diluted silane

and hydrogen. The collector part of the apparatus is placed directly under the tube and the reactor and collector area can be filled with inert gas up to the atmospheric pressure for sample extraction. The size and the PL wavelength of the samples were tuned by changing the composition of the synthesis gases as detailed in Table 1. The estimated residence time of the forming nanoparticles in the plasma was about 15 ms. The synthesis times were 3 minutes for 2.5 mg and 10 minutes for 10 mg of H:SiQDs.

2.3. Preparation of H:SiQDs and reactant mixture under an inert atmosphere

For the subsequent reactions (hydrosilylation or plasma-induced in-liquid reactions) under an inert atmosphere, a non-commercial inert atmosphere (flow-box gases) flow box (Synth-box, 3D printed) was attached to the synthesis system (working pressure 200 kPa, set to prevent exposure to ambient conditions). In the Synth-box, a 20 ml glass vial filled with 5 ml of a given ligand liquid was purged with argon for 5 minutes using a Shenzen PINYA mini pump (max. voltage 5 V, max. flow 3 l min⁻¹) set to a flow of 1.5 l min⁻¹ powered by a DC power source (Tesla BK 127 stabilized source). The as-synthesized SiQDs were transferred to the vials and purged again for 5 minutes. The vials were then sealed with a Teflon coated cap and ultrasonicated for 15 minutes. No other purification steps were taken. This procedure is further referred to as 'inert atmosphere synthesis' (IAS).

2.4. Preparation of H:SiQDs and reactant mixture under ambient conditions

The procedure, further designated as 'air exposure synthesis' (AES), was carried out without the Synth-box. The manipulation with the liquid reactants was the same as for the inert atmosphere conditions. The crucial difference is that H:SiQDs were extracted under ambient conditions, minimizing contact with air; therefore, the estimated air exposure is 30–90 seconds.

2.5. Surface modification using plasma-induced in-liquid reactions

The plasma-induced in-liquid reactions (PILRs) were carried out using our home-built system containing an electrode system (two electrodes, the submerged electrode: Pt wire, the upper electrode: MEDOJECT needle 1.2 × 40 mm ('diameter' × 'length')), a reactor (5 ml glass beaker) for the liquid mixture and a 3D printed protection box (PILR-Box) flushed with argon to sustain stable conditions without oxygen. For modification, the reactor was filled with 3 ml of the reaction mixture. The used geometry of the plasma discharge, for the induction of the reactions, is point-to-plane, with one submerged electrode and a second one 2.5 mm above the liquid. The discharge is operated in the pulse regime, due to the usage of ballast impedance, which contains parallel connection of a 10 MΩ resistor and a capacitor system of an overall capacity of 250 pF, generating transient spark discharge. Plasma discharge was generated using a high voltage DC power supply (MCP M10-HV10000A)

Table 1 Parameters of the synthesized SiQDs (nominal RF source power was set to 150 W in all samples). Sample labeling reflects their sizes. Residence times (t), the flows of the precursor gases (1% SiH_4 in the Ar mixture, H_2, Ar), sizes as determined by different methods, XRD-derived lattice parameter a, PL maxima and QYs are listed. The sizes are shown as mean size $\pm$FWHM/2 to represent the width of the distributions.

Label	t (ms)	Mixture (sccm)	H_2 (sccm)	Ar (sccm)	XRD size (nm)	$a^{a,b}$ (Å)	Size^{c,d} (nm)	d_{DLS} (nm)	PL pos. (eV)	QY^c (%)
EL-SiQDs	28	80	0	0	4.0 ± 1.2	5.426 ± 0.002	6.3/4.8	25.0 ± 1.5^e	1.25	—
L-SiQDs	23	80	10	0	3.4 ± 1.1	5.427 ± 0.002	5.5 ± 0.6	19 ± 5	1.32	9.6 ± 0.7
M-SiQDs	17	80	40	0	2.8 ± 0.9	5.429 ± 0.004	4.0 ± 0.6	12.0 ± 2.5	1.43	19 ± 3
S-SiQDs	12	40	100	40	1.9 ± 0.8	—	2.44 ± 0.22	8.7 ± 0.8	1.76	5.2 ± 0.5

^{a} NIST standard Si standard reference material a = 5.43102 Å. ^{b} The lattice parameter for the S sample could not be precisely refined due to extremely broad diffraction peaks. ^{c} Measured for dodecyl:SiQDs. ^{d} Derived from HRTEM measurements. ^{e} Derived from the first DLS band.

and the used voltage ranged from 3 to 9.5 kV. To ignite and maintain stable plasma discharge and conditions, the flow of the inert argon gas was set to 1 ml min^{-1} (using the Shenzen PINYA mini pump). For successful modification of the surface of H:SiQDs, the overall reaction time was set to 35 minutes. The 35 minutes were divided into two intervals: (i) initiation (5 minutes), the voltage was set for 3 kV and less energetic discharge was ignited to generate ions and a more conductive environment; (ii) propagation (30 minutes), the voltage was set to 9 kV and highly energetic discharge was ignited. The reaction mixture was not mechanically stirred; the mixing during the reaction was caused by the plasma pulses, which generate flows in the liquid. The reaction was monitored through the quartz PILR-Box windows by visual detection of PL excited with a laser pointer at 405 nm, 50 mW. As liquid reactants octan-1-ol, ethanol, acetic acid and phenol were used, leading to bonding of the corresponding alkoxy groups: octoxy, ethoxy, acetate and phenoxy. The SiQDs reacted with octan-1-ol were purified as the low volatility of octan-1-ol prevented further characterization. The purification was carried out using an ultracentrifuge; propan-2-ol/acetonitrile were used as the solvent/antisolvent pair. The ultracentrifuge was set for all samples to 195 500 × g for 120 minutes due to the high viscosity of octanol. The purified SiQDs were stored in 1-propanol (isopropyl alcohol (IPA)). The remaining SiQDs were kept in the original liquid (not purified). The purification process was performed three days after the reaction process, as the maceration of the SiQDs in the reaction mixture in an argon filled vial under sealed conditions was observed to lead to a better purification material yield and better optical properties. The argon atmosphere and sealed conditions prevent the exposure to air and humidity, and therefore prevent oxidation.

2.6.   Thermal surface modification by dodecyl groups

The glass reaction vial with the reaction mixture (H:SiQDs with 1-dodecene) was placed on a hot plate with an aluminum heating nest. The temperature was set to 190 °C and the reaction was carried out for 12 hours while stirring. The temperature of the samples was monitored using an FLIR camera (FLIR E4). After the reaction, the samples were purified using two centrifugation/precipitation cycles in an ethanol/hexane solvent/antisolvent pair in a 3 : 1 ratio. The used centrifuge was a Beckman Coulter Optima Max-XP with a TLA-110 fixed-angle

rotor equipped with 3.2 ml open-top thick-wall polypropylene centrifuge tubes. The centrifugation parameters varied based on the SiQD size from 48 900 × g for 35 min for the largest SiQDs to 195 500 × g for 45 min for the smallest SiQDs. The purified samples with dodecyl capping (dodecyl:SiQDs) were then dispersed and kept in toluene. The purification process was done three days after the reaction process, the same as in the case of the PILR samples, as the maceration of the SiQDs in the reactant mixture was observed to lead to a higher material yield of the purification and better optical properties. The maceration process was done in the sealed reaction vial filled with argon without the extraction of the dispersion of SiQDs in 1-dodecene to prevent air and humidity contact with the dispersion.

2.7.   Etching of SiQDs

For etching of the synthesized SiQDs, 2.5 mg of the dry SiQD powder was mixed with 1 ml of ethanol. 5 ml of HF was added and the mixture was stirred for 45 minutes under standard laboratory conditions. Then SiQDs were extracted into toluene. Specifically, 4 ml of toluene were added and the mixture was vigorously stirred for 5 minutes. After another 5 minutes without stirring, the ethanol and water-based phases separated with SiQDs dispersed in the toluene phase. The toluene phase was collected.

2.8.   Structural and chemical characterization of SiQDs

A Nicolet (Thermo Scientific) iS50 FTIR spectrometer was used for the infrared absorption analysis of the surfaces. The acquisitions were carried out using the attenuated total reflectance (ATR) diamond crystal. The collection conditions were set for 256 scans with 2 cm^{-1} resolution. The OMNIC software was used for data recording, baseline subtraction and signal processing.

The sizes and their distributions of the SiQDs were determined using XRD and high-resolution transmission microscopy (HRTEM). The used HRTEM is a JEOL 2200 FS using a ZrO/W FEG operated at 200 kV. The data from the HRTEM were analysed manually using the ImageJ software (we verified that the extracted histograms are independent of the person carrying out the analysis). X-ray diffraction (XRD) experiments were conducted using a SmartLab X-ray diffractometer (Rigaku, Japan) equipped with a 9 kW rotating Cu

anode, Johansson monochromator (producing monochromatic radiation with wavelength λ = 1.5406 Å), and 5° Soller slits to eliminate axial divergence in both primary and diffracted beams. The diffracted intensity was measured using a 2D hybrid pixel, single photon counting HyPix 3000 detector. The measurements were performed in a para-focusing Bragg–Brentano geometry with constant irradiated area mode, covering the 2θ range of 15°–150° with a step size of $\Delta 2\theta = 0.05°$ and a scan speed of 2° min^{-1}. The XRD data were analyzed using the whole powder pattern fitting technique (Rietveld method) to derive structural parameters such as crystallite sizes, lattice strain, and lattice defects of the nanocrystalline Si phase. The computer program MStruct[61] was employed for the fitting. The size distribution of coherently diffracting domains (crystallite size) was modeled using the lognormal distribution.

2.9.   Characterization of dispersions

The dispersion was characterized using the Zetasizer Nano ZS (Malvern Panalytical) dynamic light scattering (DLS) apparatus equipped with a helium–neon laser (633 nm). The scattering angle of 173° was used. The colloidal SiQDs were filtered using 450 nm PTFE syringe filters (diameter 25 mm, FiltraTECH) and pipetted into a quartz cuvette for colloids in toluene or a disposable polystyrene cuvette for other solvents. Every colloid was analysed 3 times for 50 runs (duration of one run: 10 s). The refractive index of SiQDs (3.50), toluene (1.496), ethanol (1.360), octan-1-ol (1.427) and propan-2-ol (1.390) and the viscosity for the solvents were used (0.56 mPa s (298.15 K), 1.1 mPa s (298.15 K), 7.36 mPa s (293.15 K), and 2.32 mPa s (298.15 K)). The number-weighted sizes were acquired using the fitting of the autocorrelation function by the in-built software running in the size measuring option.

2.10.   Optical characterization

Steady-state photoluminescence (PL) spectroscopy was carried out using non-commercial systems operated in a 90° geometry with the SiQD colloids in the liquid form in a quartz cuvette. As an excitation source a continuous laser beam at 325 nm with a power of 2.3 mW of a He–Cd laser system (KIMMON IK series) was used. The optical signal from the sample was coupled into UV optical fibers connected to the spectrograph Shamrock 300i (Andor, Oxford Instruments) equipped with the EMCCD camera Newton 971 (Andor, Oxford Instruments). The collection conditions were 200 accumulations with a 0.2 s acquisition time. To prevent the reabsorption, the colloids were diluted to 40% transmission. All presented spectra are corrected for the spectral response of the whole system (correction based on the Ocean Optics HL3 Plus calibration lamp).

QY measurements were carried out using the absolute method on a non-commercial setup, based on the Energetiq Laser Driven Light Source EQ99-X as the excitation light source and a Thorlabs IS200-4 integrating sphere. The white light excitation was fed through an MSH 150 monochromator to set the excitation wavelength and then it was coupled to the Thorlabs M28L01 optical fiber (a diameter of 400 µm, 0.39 N.

A.) using a pair of planoconvex lenses. The chosen excitation wavelength was 400 nm. For the QY measurements of the colloids, a micro-cuvette (Hellma Micro-cuvette 111.057-QS, 5 × 5 mm) with a round Teflon stopper was used. The collected signal was coupled by an optical fiber into the monochromator and detector (Shamrock 300 and a Newton 971 EM-CCD camera). The detailed acquisition protocol has been published elsewhere.[62]

The photoluminescence dynamics was measured using the Hamamatsu C10627 streak camera (reaching a temporal resolution of 15 ps) coupled with an imaging spectrometer. The SiQD colloids were excited using a femtosecond laser PHAROS (150 fs pulses, Light Conversion) coupled with a harmonics generator HiRO (Light Conversion, excitation wavelength 343 nm, and repetition rate 1 kHz). The optical signal was collected at a 90° angle. All the optical measurements were performed under room temperature conditions. The spectra were corrected for the spectral sensitivity of the whole setup.

The measured lifetimes were analyzed using a home-built Matlab code.[63] Typically, the decays were well-described by a stretched-exponential curve[60] $I(t;\lambda) = I_0(\lambda) \exp\left\{-\left(\dfrac{t}{\tau_{SE}(\lambda)}\right)^{\beta}(\lambda)\right\}$, τ_{SE} being the stretched-exponential lifetime and β the stretched-exponential parameter. The corresponding average lifetimes τ were then calculated as[60]

$$\tau(\lambda) = \frac{\Gamma(2/\beta(\lambda))}{\Gamma(1/\beta(\lambda))}\tau_{SE}(\lambda), \tag{1}$$

where $\Gamma()$ stands for the gamma function. The integrated lifetimes from Table 2 were calculated by integrating the temporally resolved PL signal over photon energies and fitting the resulting PL decay curve in the same way as above.

3.   Results and discussion

3.1.   Plasma-driven SiQDs

3.1.1.   Nonthermal plasma synthesis. SiQDs were synthesized in non-commercial flow-through apparatus in non-thermal plasma based on protocols introduced by Kortshagen *et al.*[64] In our apparatus, Fig. 1A, we introduce a tapered mid-section into the reaction glass tube, with planar electrodes placed in the tapered part. The tapered part ensures a higher density of the plasma discharge, locally increasing the energy density to ensure faster crystallization. Moreover, our system is equipped with a non-commercial 3D printed flow box (Synth-Box) filled with inert gas (nitrogen 5.0 or argon 4.7) to ensure the collection of the synthesized sample with minimal exposure to air-originating contaminants such as oxygen and water. The 3D printed design of the flow box is advantageous due to its modifiable design, compact dimensions, low manufacturing and operational costs, and easy maintenance and implementation, making it a good alternative to conventional gloveboxes.

Table 2 Optical properties of the PILR-modified SiQDs. Blue shift and PL enhancement accompanying the modification and the β parameters of the stretch-exponential fit from Fig. S7B, C and S6 are listed, together with the dark-to-bright ratios and the lifetime of the spectrally integrated PL. Simply the stretched-exponential lifetime τ_{SE} is shown, for the average lifetime τ, see Table S3

| Label	Surface type (solvent)	PL blue shift (eV)	PL rel. enh.	β	Dark-to-bright QDs (N_{dark}/N_{bright})	τ_{SE} of int. PL (µs)
L-SiQDs	Dodecyl (in TOL)	0.07	22.5	0.6	9.4 : 1	34.4 ± 0.8
	Octoxy (in OCT)	0.16	18.9	0.7–0.8	4.5 : 1	43 ± 1
	Ethoxy (in EtOH)	0.12	3.4	0.65–0.75	49 : 1	48.1 ± 0.7
M-SiQDs	Dodecyl (in TOL)	0.17	6.4	0.8	4.2 : 1	56 ± 1
	Octoxy (in OCT)	0.13	12.5	0.7–0.8	5.9 : 1	30.3 ± 0.7
	Ethoxy (in EtOH)	0.10	5.8	0.7–0.8	6.9 : 1	30.9 ± 0.5
S-SiQDs	Dodecyl (in TOL)	0.13	7.2	0.7	18 : 1	20.6 ± 0.4
	Octoxy (in OCT)	0.29	1.8	0.75	27 : 1	30.3 ± 0.7
	Ethoxy (in EtOH)	0.11	2.5	0.65–085	<30 : 1	30.9 ± 0.5
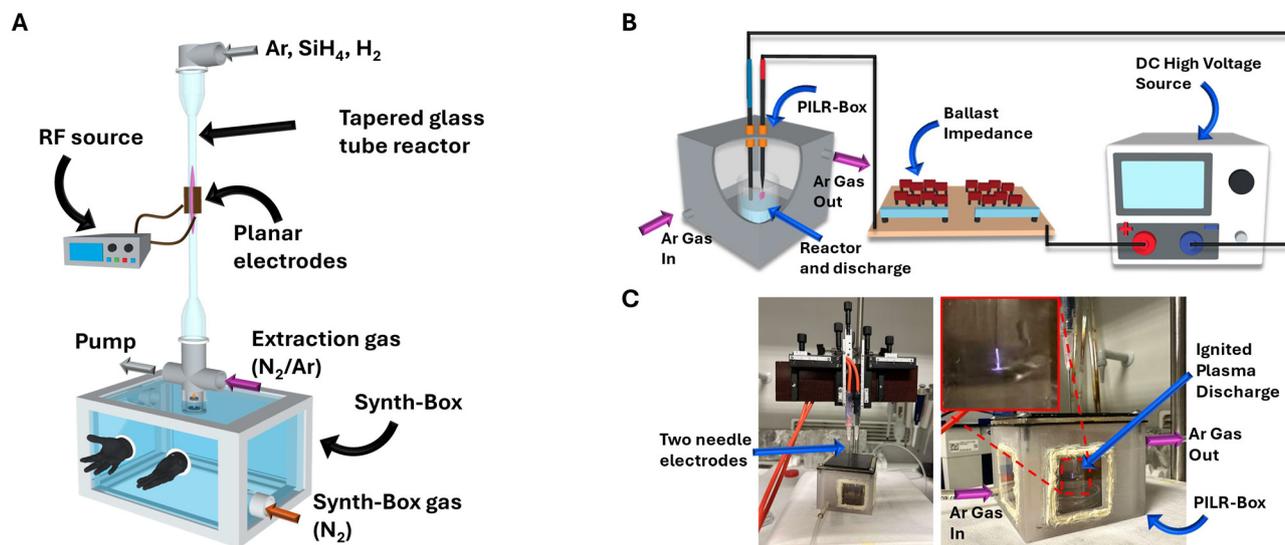
Fig. 1 All-plasma SiQDs: (A) simplified scheme of the synthesis procedure: the gas precursors (silane, hydrogen and argon) were flown into the glass tube reactor, where SiQDs were formed using an RF-powered plasma discharge. SiQDs were collected on a glass substrate and extracted into solvents in a custom-designed nitrogen flow box. (B) Simplified scheme of the PILR procedure; using a high-voltage DC source, ballast impedance and a custom 3D printed argon flow box. (C) Photographs of the working PILR system with two needle electrodes (one submerged, point-to-plane design) and burning discharge in a glass reactor.

Moreover, we optimized our system and synthesis protocols for material yield. The conversion rate of SiH₄ in the reactor reaches more than 75% based on the ratio of total weights of the precursor gases to collected SiQDs, leading to an overall yield of more than 60 mg per hour. To avoid overheating, in a high-material-yield synthesis, the generation of nanoparticles (plasma discharge ON) step is alternated with a cooling step (plasma discharge OFF) in a 3 : 1 duration ratio. The sequence can be repeated to achieve an overall process time of up to 60 minutes. With the decrease in the diameter of the synthesized SiQDs, the material yield decreases and the duration of one sequence is reduced to 5 minutes, to ensure the synthesis of SiQDs without surface burning or any other damage.

3.1.2. Size tuning. In our synthesis protocols, we introduced extensive size tuning, which is later reflected in the shifts of the maxima of the photoluminescence wavelength (see section 3.4 thereafter). The size of the synthesized nano-

particles can be tuned by the composition of the precursor gas mixture, flow rate and residence time,[36,59] see Table 1, in a wide size range between approximately 6 and 2.45 nm. Four samples, denoted as *EL-*, *L-*, *M-* and *S*-SiQDs with decreasing size, were prepared for this study.

The general model for the growth of Si nanoparticles in non-thermal plasma involves three stages of nucleation, coagulation and surface growth while maintaining sufficiently energetic conditions in the plasma to ensure crystallization.[17] In our protocols, while keeping the power setting constant to ensure high crystalline quality, the size of the produced QDs is primarily tuned by adding H₂ to the synthesis gas mixture. The increased overall flow decreases the residence time for the nanoparticles to form. At the same time, it introduces an etching-like mechanism[65] to the surface-growth phase of the nanoparticle formation, effectively competing or interfering with the growth in size. Consequently, the SiQDs synthesized

with an additional H_2 flow have a different chemical composition of terminating surface hydrides and different surface facets, as shown in our previous work.[31]

Plasma conditions for the smallest S-SiQDs are the most difficult to fine-tune as the right balance between conditions energetically ensuring crystallization, a sufficiently short residence time and chemical processes during the synthesis need to be reached. The S-SiQD sample was optimized for reasonable optical performance, which is typically poor in very small SiQDs. Even though the small size was primarily reached by the same mechanisms as for the larger QDs, i.e. by using the highest H_2 flow rate, in this sample, half of the flow of the 1% SiH_4 mixture was replaced with pure Ar. This setting slightly increased the amount of energy-supplying argon in the synthesis gas at the expense of silicon available for nanoparticle formation. Potentially, such fine-tuning might also influence the coagulation phase during the formation of nanoparticles and act as a selection mechanism for sufficiently crystalline small SiQDs. Therefore, by increasing the H_2 flow accompanied by potential fine-tuning of the synthesis gas composition, we can obtain a broad range of core sizes (2.45–6 nm), while keeping a reasonable degree of crystallinity (see section 3.3.2 thereafter) and optical performance (see section 3.4 thereafter) even for the smallest QDs. However, size tuning also influences the material yield, which is ≈3× lower for the S-SiQD than for the L-SiQD sample.

3.1.3. Plasma-induced in-liquid surface modification. Plasma synthesis produces hydride-terminated SiQDs (H: SiQDs), which are unstable in air. The most common surface-modification procedure for SiQDs to ensure stability, dispersibility and photoluminescence is hydrosilylation. Here, we introduce plasma induced in-liquid reactions (PILRs) as an alternative approach. PILRs have so far been only scarcely studied and are therefore much less understood, but they have the potential to (i) broaden the range of available ligands, which are limited by the requirement of the initial double bond in the case of hydrosilylation, and (ii) significantly shorten the reaction times. During a PILR treatment, the nature of the generated reactive species to be attached to the surface depends significantly on the surrounding atmosphere,[47] which interacts with and thus influences the treating liquid even more than in the conventional hydrosilylation. Therefore, unlike in previous studies,[42,44–49] we carry out the PILR modifications under a controlled atmosphere. This technical modification ensures better repeatability and the possibility of using less polar liquids as the source of reactants.

Therefore, our setup consisted of a minimalistically designed 3D printed protection reactor box with a screw-attached and sealed lid (PILR-Box), see Fig. 1B. The box contained one 5 ml reactor and was flushed throughout the entire reaction process with Ar gas. The as-synthesized SiQDs were collected in a Synth-Box attached to the synthesis system, placed in a 20 ml glass vial filled with an argon-purged reactant liquid and a Teflon cap was screwed on the top of the vial. Then, the dispersion in the glass vial was taken out of the

Synth-Box and 3 ml of the dispersion were pipetted into a 5 ml glass reactor placed in the PILR-Box. The PILR-Box was sealed, with the electrodes in place in the glass reactor, and flushed with argon (flow: 1 l min⁻¹). After the flushing cycle, the plasma discharged was ignited, see Fig. 1C. The overall reaction process time for all ligands was 35 minutes. Next, the PILR-Box was flushed with argon, unsealed and the dispersion of the modified SiQDs was extracted. The after-reaction dispersions for M- and L-SiQDs in reactants are shown in Fig. S1A and S1B, respectively.

We tested a set of liquids to cover the interval from polar to non-polar molecules to achieve dispersions in different environments, in particular ethanol (EtOH), acetic acid, octan-1-ol (OCT), the toluene–phenol mixture and 1-dodecene. The molecules were also chosen to be conductive, so the plasma discharge can burn towards them. While PILR modification occurred in all the liquids, the best results ensuring surface stabilization and photoluminescence were achieved using EtOH and OCT as a reactant and therefore, these two types, labeled as etoxy:SiQDs and octoxy:SiQDs, will be discussed in more detail. The summary of the influence of other passivants is provided in Table S1.

In short, acetate derived from acetic acid was tested as a highly polar ligand. Significant PL enhancement (14×) was achieved, but the extraction from the reactant turned out to be difficult. As for the toluene/phenol mixture, where toluene was used to dissolve solid phenol, a non-polar environment and aromatic termination were targeted. However, the PILR treatment of this mixture was problematic due to low conductivity resulting from the non-polar nature and led to a mere 1.5× PL enhancement. Actually, a larger PL enhancement was achieved when the SiQDs were solely left to macerate in the mixture. Also, the purification process was problematic due to the solid state form of phenol. Lastly, non-polar 1-dodecene was also used as a PILR reactant. In this way, a moderate 2× PL enhancement was achieved. Once again, the PILR procedure was complicated by the instability of the discharge because the non-conductive nature of 1-dodecene and PILR-treated dodecyl:SiQDs exhibited similar PL properties as H:SiQDs simply left to macerate in 1-dodecene. In this regard, the conventional hydrosilylation (see section 3.2) was clearly superior. Therefore, our experiments demonstrate that the PILR procedure is not ideal for non-polar ligands. However, as non-polar termination is easily achievable through well-established hydrosilylation techniques, PILR can serve as an important additional tool to cover the spectrum of more polar ligands, if the protocols are further developed into a more matured state.

As a sidenote, when the octan-1-ol (OCT) liquid was used as the reactant, the sample needed to be purified for the FTIR analysis, which would otherwise be complicated in a low volatile liquid. The purification process was carried out via one centrifugation/precipitation cycle in a propan-2-ol/acetonitrile solvent/antisolvent pair with propan-2-ol (IPA) as a final (storage) solvent. IPA was chosen as the storage solvent due to its mildly polar nature; however, the modified octoxy:SiQDs do not disperse in IPA ideally.

3.2. Thermal hydrosilylation

To serve as a reference, conventional thermal hydrosilylation with dodecyl groups (dodecyl:SiQDs) was carried out for all sizes of SiQDs in this study. Notably, in contrast to synthetic approaches involving HF etching,[21,67] in NTP synthesis the QDs are produced in the form of dry powder which needs to be mixed with the reactant liquid. With the aim of keeping the procedure as simple as possible, we chose the thermally-initiated hydrosilylation over the radically- and photochemically-initiated hydrosilylation, due to its versatility to all SiQD sizes and lower sensitivity to air and humidity. Moreover, we tested the effect of short exposure to normal atmosphere on the outcome of the hydrosilylation-based modification. The simplicity of the process involved only the storage of the reagents over molecular sieves and purging of the reaction vials and liquids with argon prior to the introduction of SiQDs.

Therefore, we compared two approaches, namely SiQDs transferred to liquid-containing vials in the protected atmosphere in Synth-Box ('inert atmosphere synthesis' or IAS, see section 2.3) with those undergoing a short air exposure of approx. 30–90 seconds necessary for the dry powder to be dispersed in the reactant liquid outside of the Synth-Box ('air exposure synthesis' or AES, see section 2.4). The hydrosilylation reaction was than performed under standard laboratory conditions without any additional atmosphere control equipment (see section 2.3) in contrast to the traditionally employed Schlenk line-based systems.[16,35]

Even naked-eye observation of the dispersion of modified SiQDs revealed notable differences between the two approaches. Whereas the IAS approach led to transparent orange-yellow dispersions, see Fig. S1A for the corresponding photos, the dispersions of AES-modified SiQDs were much more opalescent (for photos, see Fig. S1A), implying that non-negligible oxidation-induced agglomeration occurred despite the short air exposure.

Thus, we put forward a slightly simplified version of thermal hydrosilylation carried out in an argon-filled closed container using pure 1-dodecene purged with argon as the reactant, without the freeze–pump–thaw degassing cycles or any other protective-atmosphere equipment (inert atmosphere, Schlenk lines) or purification processes while reaching reasonable optical performance (see section 3.4 thereafter). As a contrast to this simplification step, we show that even a very short-term exposure of the dry SiQD powder to air and humidity needs to be avoided if hydrosilylation is to proceed successfully and a protective-atmosphere Synth-Box filled with non-dried 5.0 purity nitrogen is a necessary minimal requirement for the collection of the sample.

3.3. Structural and chemical characterization

3.3.1. HRTEM analysis.
HRTEM measurements were performed as a primary probe to the size of the synthesized QDs, using purified dodecyl:SiQDs to ensure dispersibility critical for HRTEM imaging.[66] Bright-field TEM images were acquired for all sizes of dodecyl:SiQDs from Table 1, see Fig. 2A for a representative example and Fig. S3 for other measurements. These HRTEM images were used to determine the histograms of sizes with mean values ranging from 2.4 to 6.3 nm and FWHM/2 of ≈10–15%, see Fig. 2B. Due to their high symmetry along the mean value, the histograms of *L*-, *M*- and *S*-dodecyl:SiQDs were fitted with one Gaussian curve. In contrast, the distribution of *EL*-dodecyl:SiQDs seems bimodal and was thus fitted with two Gaussian bands. The ratio of integrated areas of these two bands is 3 : 1 in favor of the larger SiQD size.

The presence of a symmetrical distribution of sizes is an atypical, although possible,[68] feature, because sizes of nanoparticles often exhibit asymmetry with a larger-size tail, commonly approximated by a log–normal distribution.[69] Potentially, the symmetrical size distribution can be tied to the extremely short times needed for particle formation (residence times 10–30 ms) and the suppression of agglomeration of the forming QDs due to negative charging in the plasma.[64] Another notable feature here is the bimodal distribution of the largest SiQDs synthesized without an additional H_2 flow. This qualitative difference between the largest SiQDs and the smaller ones suggests that the additional H_2 flow might in fact promote the coagulation of the forming QDs, consequently yielding a single-size distribution. Lastly, we want to highlight the wide range of sizes accessible with our protocols. The smallest *S*-SiQDs are among the smallest SiQDs fabricated by the LP-NTP.[2,15,36]

For the purposes of the comparison with XRD (see section 3.3.2 thereafter), where the change of the underlying shape of the size distribution for the analysis is non-trivial, the HRTEM-derived size histograms were refitted with a lognormal distribution, see Fig. S4 and Table S2. The Gaussian fit gives a consistently higher R^2, implying a better agreement with the fitted data, and therefore, the size distribution of the studied samples is represented by these Gaussian fits in the following text. However, realistically, the difference between the Gaussian and lognormal distributions both in terms of the shape and the determined values is marginal. Therefore, the parameters of the HRTEM distributions can be directly compared with the XRD-derived ones.

3.3.2. X-ray diffraction.
The as-synthesized SiQDs with minimized air exposure underwent X-ray diffraction (XRD) measurements to characterize their crystalline quality and sizes as displayed in Fig. 2C. Based on the analysis using the MStruct package[70] assuming a lognormal crystallite size distribution, the samples contain a nanocrystalline silicon phase (space group $Fd\bar{3}m$, no. 227). Additionally, a fraction of an amorphous phase (or disorganized atoms) is also present, as indicated by the broad peak between the diffraction angles of 15–40°. The refined, number-weighted crystallite size distributions are shown in Fig. 2D, their mean values and lattice constants are listed in Table 1. Lattice strain increases with decreasing crystallite sizes, accompanied by an increase in stacking faults. Across all samples, the lattice parameter is slightly smaller than the tabulated value for bulk Si. The difference ranges between 0.04 and 0.09%, getting closer to the bulk
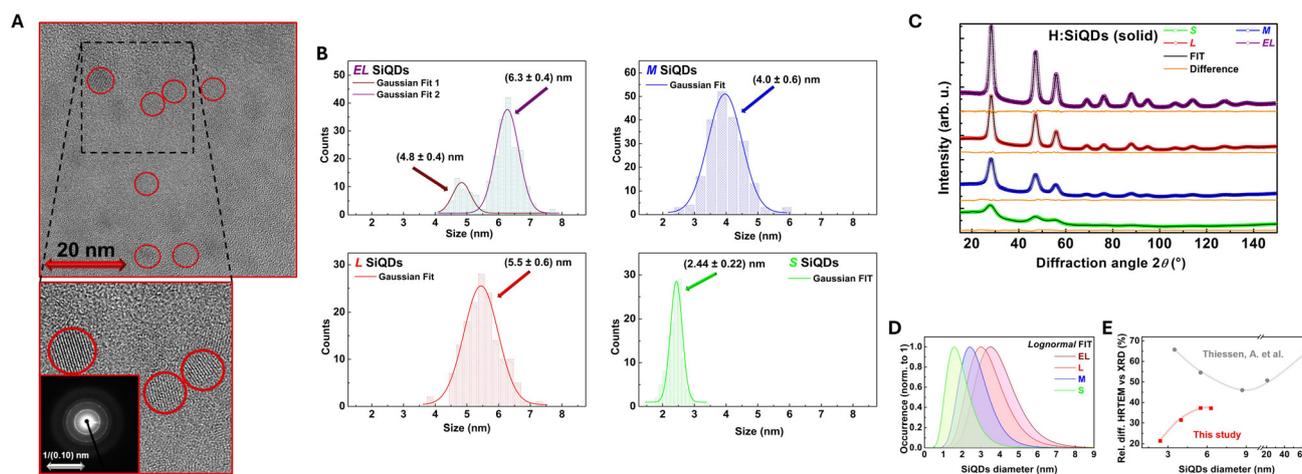
Fig. 2 SiQDs' size and structure: (A) a representative example of a bright-field HRTEM image of *L*-dodecyl:SiQDs produced using the non-thermal plasma system for the synthesis and the *IAS* hydrosilylation approach. (B) Histograms of sizes of dodecyl-terminated samples from Table 1 derived from HRTEM images. (C) Measured (open circles), calculated (solid lines) and difference (yellow line at the bottom) X-ray diffraction patterns of the studied samples. For the quantification of the size and lattice constant, see Table 1. (D) Lognormal fit of the diameter distribution acquired from XRD measurements for the studied SiQDs. (E) Comparison of the difference of SiQDs' mean sizes derived from XRD and HRTEM measurements, comparison with the dependency observed by Thiessen, A. *et al.*[66] is included.

value for smaller QDs. As XRD probes a macroscopic amount of QDs, the perfect agreement between the measured diffractogram and the fit shown in Fig. 2C implies that the XRD-derived size distribution in Fig. 2D represents the volumetrically dominant fraction, and no significantly larger nanoparticles are present.

Sometimes, the Scherrer formula is used to determine the mean size[68] instead of the whole powder pattern fitting (WPPF) method applied here. In general, in nanocrystalline materials, WPPF is more reliable for crystallite size determination than the Scherrer method because it accounts for the full complexity of peak broadening effects. The Scherrer method, while simple, assumes that broadening arises solely from the small crystallite size and typically uses a single peak, ignoring contributions from microstrain and peak asymmetry, all of which are significant in nanomaterials. In contrast, WPPF fits the entire diffraction pattern using a physically meaningful model that simultaneously considers size, strain, and instrumental effects across multiple peaks. This holistic approach provides a more accurate and representative measurement of crystallite size in nanocrystalline materials, where line broadening is often substantial and affected by several overlapping factors. A comparison of the application of WPFF and the Scherrer formula to our samples is shown in Table S2, where the Scherrer formula systematically yields somewhat larger sizes, however, the difference is not significant in our case, usually around 10%. This relatively small difference is caused by the well-defined size distribution in our samples; a potential presence of, *e.g.*, larger particles resulting in a bimodal distribution would lead to a more significant disagreement between the WPPF- and Scherrer-derived size distributions.

To further confirm the crystalline quality of the produced SiQDs, we tested if they can withstand HF etching in ethanoic, ≈40% HF (see section 2.7). The procedure was carried out in both freshly synthesized H-terminated and slightly pre-oxidized SiQDs. After 45 minutes of etching, a highly murky dispersion of toluene-dispersed SiQDs was collected for all the produced sizes of QDs. An exception was the pre-oxidized *S*-SiQD sample, which dissolved in the etching mixture and the QDs were retrieved. The dissolution of this sample was most likely due to very small size exacerbated by the oxidation (freshly synthesized *S*-SiQDs withstood the procedure). This resistance to HF confirms the high crystalline quality of the produced SiQDs.

3.3.3. HRTEM *vs.* XRD. The XRD-derived size distributions systematically yield smaller mean sizes. In general, a difference in the two techniques is to be expected, as XRD probes only the coherently diffracting domains, whereas HRTEM provides a more direct measurement of the QD's outer dimensions.[71] This difference is often attributed to an "amorphous" or "disordered" surface layer or shell.[66,67] In our study, though, the surface layer is significantly thinner, see Fig. 2E, and its relative thickness decreases with decreasing size. The thinner surface layer in our samples might suggest QDs of higher structural quality, even though such a comparison is potentially sensitive to the detail of the applied XRD analysis. Also, at least the *EL*- and *L*-SiQDs investigated here were shown to support surface faceting.[31] Thus, we do not attribute the difference between XRD- and HRTEM-derived sizes simply to an "amorphous" surface layer, but to a surface layer with a lower degree of crystalline order as the structural ordering in QDs can be expected to change gradually rather than switching between two states defined for a macroscopic crystal (crystalline *vs.* amorphous).[54]

The comparison of HRTEM- and XRD-derived size distributions then gives evidence of much more pronounced asymmetry and larger width detected by XRD (approx. 10 and 30%

with respect to the mean size for the HRTEM and XRD, respectively). In principle, the differences between the shapes of the XRD- and HRTEM-derived size distributions could be connected to the size-dependent shape thickness as plotted in Fig. 2E, but the corresponding discussion is beyond the scope of this article.

3.3.4. FTIR analysis. FTIR spectroscopy was carried out to analyze the chemical composition of the attached ligands. These measurements were performed for all sizes with the same result; therefore, we present one representative spectrum of one SiQD size.

Hydrogen-terminated and oxidized SiQDs reference. In the FTIR spectra of the as-synthesized H:SiQDs, see Fig. 3A, the typical broad SiH_x (x = 1, 2, and 3) stretching vibration appears with three well-resolved main bands located at 2085, 2105 and 2140 cm^{-1}, assigned to the SiH_3, SiH_2 and SiH stretching modes,[31,72–75] respectively. These bands are accompanied by weaker ones in the same region corresponding to the SiH and SiH_2 stretching (see Fig. 3A). Moreover, the well-resolved bands in the 600 to 700 cm^{-1} region correspond to the deformation and wagging vibration of SiH_x.[31,76,77] The two strong peaks at 905 and 857 cm^{-1} are also typical of the plasma-synthesized H:SiQDs.[31] The weak round broad signal with a maximum[78–80] at 1080 cm^{-1} can be attributed to the stretching of the Si–O–Si bridge, implying weak oxidation of the surface caused by the exposure to atmospheric oxygen during the FTIR measurement. As a reference, an air-oxidized O:SiQD sample is also

included (Fig. 3A). The O:SiQD sample exhibits a fully oxidized surface, with a missing signal in the SiH_x stretching region at 2000–2200 cm^{-1} as well as the missing SiH_x deformation vibrations in the 600 to 700 cm^{-1} region. The fully oxidized surface is characterized by the broad band in the interval from 1200 to 900 cm^{-1} corresponding to the Si–O–Si stretching vibrations,[81] with a maximum at 1050 and a shoulder at 1160 cm^{-1}.[78–80]

Hydrosilylated SiQDs. In the FTIR spectra of dodecyl:SiQDs after both *AES* and *IAS* hydrosilylation with 1-dodecene, the SiH_x stretching vibrations were no longer detected, implying that the hydrides on the surface were substituted with organic ligands. The presence of the long alkyl chains was evidenced by the vibrational signals from the CH_2 groups, represented by the asymmetric and symmetric CH_2 stretching vibrations[82] at 2920 and 2850 cm^{-1}, respectively, as well as by the deformation at 1440 cm^{-1} and the rocking vibration at 720 cm^{-1}. The terminal CH_3 presented as symmetric and asymmetric valence stretching vibrations at 2960 and 2865 cm^{-1},[35,81,82] accompanied by the degenerated deformation mode at 1460 cm^{-1} and the symmetric umbrella deformation of the terminal CH_3 at 1375 cm^{-1}. The symmetric and asymmetric stretching vibrations were present as shoulders to the CH_2 stretching vibrations due to the ratio of 1 to 11 of CH_3 to CH_2 groups in the chain. The successful bonding of the 12C alkyl chain to the SiQDs' surface was evidenced by the absence of the asymmetric vibration of the non-attached 1-dodecene
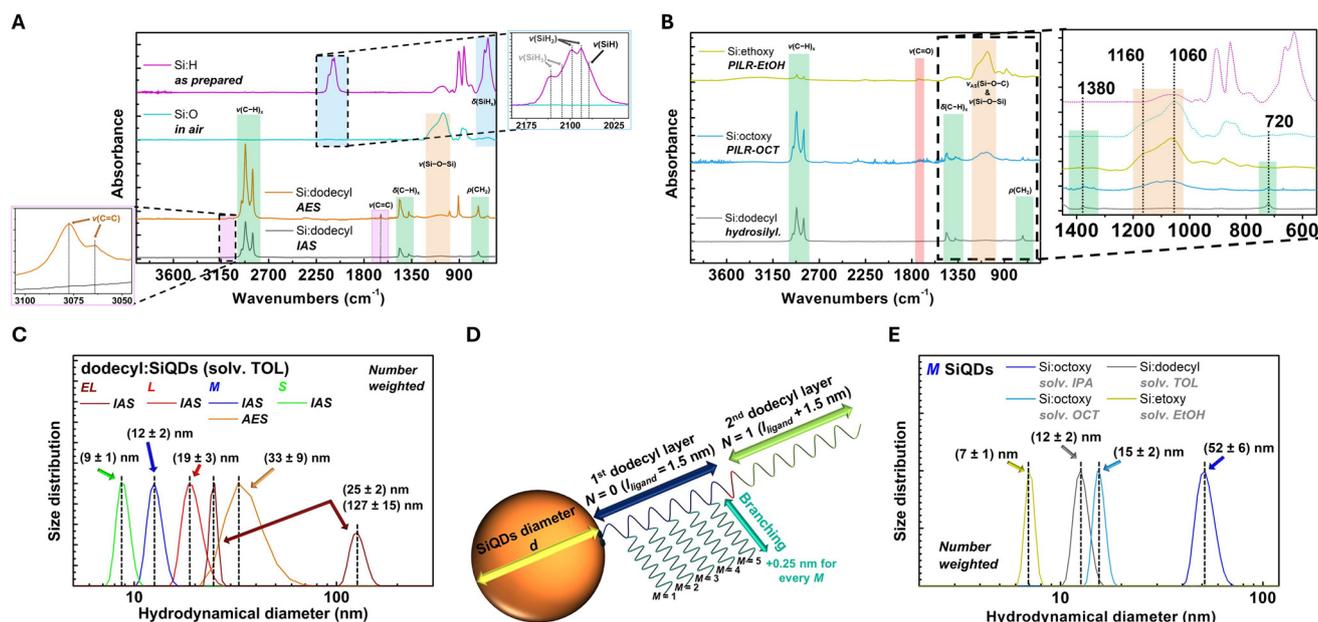

Fig. 3 Modified SiQD surface: (A) comparison of the SiQDs' surfaces of the as-synthesized, naturally oxidized and dodecyl:SiQDs prepared by both the inert atmosphere synthesis (*IAS*) and air exposure synthesis (*AES*) approaches (see section 3.2 for details). (B) Comparison of the SiQDs' surfaces modified by conventional hydrosilylation (dodecyl:SiQDs), the PILR method using the ethanol (ethoxy:SiQDs) and octanol liquids (octoxy:SiQDs). The detailed area from 1400 to 600 cm^{-1} was expanded for an easier comparison with the FTIR spectra of Si : H and Si : O (color corresponds to (A)). (C) DLS measurements of dodecyl:SiQDs from Table 1, including the comparison of the *ILS* and *AES* methods for the *M* sized sample. (D) Schematic illustration of the dodecyl bonding to the SiQDs' surface (see eqn (2)). (E) DLS measurements of *M*-dodecyl:SiQDs, *M*-etoxy:SiQDs and *M*-octoxy:SiQDs showing the dispersibility potential of selected surface terminations.

terminal CH$_2$ group on a double bond at 3080 cm^{-1} and the stretching of the C=C bond at 1675 cm^{-1}, see the corresponding dodecyl:SiQDs *IAS* spectrum (Fig. 3A).

FTIR spectroscopy also revealed subtle differences between the *AES* and *IES* protocols (section 3.2), see again Fig. 3A. First, the *AES* approach led to a slightly more intensive signal from the Si–O–Si vibration (around 1070 cm^{-1}), implying a more oxidized surface. Although the oxidation level in the *AES*- and *IAS*-hydrosilylated SiQDs was, according to the FTIR spectra, minuscule, it was sufficient to induce interparticle aggregation, in agreement with the less transparent and more opalescent liquid obtained by the *AES* hydrosilylation process. The second difference was represented by the two weak peaks at 3080 cm^{-1} and 1675 cm^{-1} in the dodecyl:SiQDs (*AES*) samples, originating from the asymmetric vibration of the terminal CH$_2$ group on a double bond and the stretching of the C=C bond, respectively. We tentatively attribute these peaks to a dodecene capsule around the agglomerates of QDs in the *AES* samples. This could imply that the thermal hydrosilylation using the *AES* procedure was carried out partially, due to the oxidized surface, resulting in aggregation and a smaller number of reactive sites.

Octoxy-modified SiQDs. The PILR-modified octoxy:SiQDs underwent FTIR analysis after purification and redispersion in IPA, see Fig. 3B. In octoxy:SiQDs, the absence of the 2000–2200 cm^{-1} SiH$_x$ (x = 1, 2, 3) stretching vibrations confirmed that all the surface SiH$_x$ reacted. The dry surface of the octoxy:SiQDs is terminated with the long alkoxy chains represented by the strong signal at 2920 and 2850 cm^{-1} from CH$_2$ vibrations, accompanied by a weaker signal at 2960 and 2860 cm^{-1} from the terminal CH$_3$ groups.[82] The relatively high intensity of the FTIR bands of the internal carbons in the alkoxy chain is due to the length of the carbon chain, being comparable to the corresponding signal in hydrosilylated dodecyl:SiQDs. The bonding of the octoxy (alkoxy) group occurs *via* an Si–O–C bridge and typically manifests from 1060 to 1160 cm^{-1}. Unfortunately, in this region, the Si–O–Si vibrations are also present,[83] complicating the analysis. A shift of the 1060 to 1160 cm^{-1} FTIR band in octoxy:SiQDs when compared to a reference sample of fully oxidized SiQDs likely indicates bonding to a lighter atom and thus the Si–O–C bridge. The lack of any alcohol-related signal indicates that the purification process was successful and confirms that the detected alkoxy chains are indeed attached to SiQDs through Si–O–C bridges, as supported by the signal in the 1200–950 cm^{-1} range.[82,83] The 1200–950 cm^{-1} spectral region is likely a mixture of Si–O–Si and Si–O–C bridge vibrations, indicating partial oxidation and thus a mixed octoxy-terminated and oxidized surface of octoxy:SiQDs.

Ethoxy-modified SiQDs. The PILR-modified etoxy:SiQDs were characterized in the original solvent. Again, the absence of the 2000–2200 cm^{-1} SiH$_x$ (x = 1, 2, and 3) stretching vibrations in the etoxy:SiQD spectra confirmed that all the surface SiH$_x$ reacted, see Fig. 3B. Furthermore, the weak signal at 2920 and 2850 cm^{-1} originating from the symmetrical and asymmetrical vibrations of the CH$_2$ and CH$_3$ groups, together with a weak

signal at 1380^{-1} from the terminal CH$_3$ group, can be attributed to alkoxy chains. Similar to octoxy:SiQDs, the bonding of the ethoxy (alkoxy) group occurs *via* an Si–O–C bridge as is indicated by the slight shift of the 1060 to 1160 cm^{-1} FTIR band. However, when compared to octoxy:SiQDs, the contribution of surface oxide is higher, as the 1060–1160 cm^{-1} band in etoxy:SiQDs has a shape typical of surface oxide on SiQDs. Additionally, a weak signal at 1720 cm^{-1} from the stretching vibration of C=O in combination with a broad signal at 3250 and around 1340 cm^{-1} from CO–O– groups can be attributed to acetic acid, which can be produced in the interaction of plasma with EtOH.[84,85] The weak signal from 3400 to 3100 cm^{-1} from the O–H stretching is assigned to the residues of the acetic acid and not evaporated ethanol. Therefore, the PILR-modified etoxy:SiQDs are terminated with a mixture of Si–O–C-bonded ethoxy group, surface oxide and acetate groups.

3.3.5. DLS analysis and discussion of size distributions. In contrast to HRTEM, DLS measurements (represented by number weighted distribution), if carried out diligently,[86] provide ensemble-averaged information inspecting a very large number of nanoparticles. Our DLS measurements (Fig. 3C) show that the hydrodynamical diameter (d_{DLS}) obtained by DLS is larger than the HRTEM derived size. The larger d_{DLS} is caused by the surface bonding of the ligands undetectable with HRTEM, which form a solvation shell around the QD in the liquid. The size of the solvation shell in general depends on many parameters, most notably on the chain length and structure of the surface ligand. Therefore, by comparing HRTEM- and DLS-derived sizes, we can obtain a quantitative estimation of the thickness of the ligand shell. The analysis we provide here aims to characterize potential ligand polymerization and inter-particle agglomeration.[36,87,88] Quantitatively speaking, the very simple analysis we put forward is inevitably linked to a margin of error as it does not explicitly account for solvent–particle interactions or a potential formation of irreversible aggregates due to incomplete surface functionalization and subsequent partial oxidation. However, our quantitative estimates explicitly take into account this margin of error by providing a range of values. Moreover, our conclusions are not solely based on the simple quantitative estimate, but are drawn based on a discussion taking into account both the shapes of the HRTEM- and DLS-derived size distributions and the polarity of the solvent, which is closely linked to the solvation shell thickness.[89] Consequently, our conclusions regarding the degree of oligomerization and agglomeration are valid despite the simplifications assumed in our quantitative analysis.

Hydrosilylated SiQDs. Hydrophobic ligands in non-polar solvents, such as dodecyl groups in toluene, tend to be fully extended,[89] therefore, we can simply assume the geometrically derived ligand chain length in our analysis. The overall bonded length for the termination with a single layer of fully extended dodecyl groups on each side of the QD is around 1.5 nm. Due to the thermal mechanism of the hydrosilylation process, oligomerization of the ligand can occur.[36,87,88] The

mechanism of oligomerization is based on branching of the first bonded dodecyl group due to the formation of a radical after the opening of the terminal double bond on 1-dodecene and the subsequent bonding onto the SiQD surface. Oligomerization can then gradually proceed on the 4th, 6th, 8th and 10th carbon on the dodecyl ligand. On the 12th C, the second layer of the dodecyl ligand can be attached.[36,87] The branching process can be stopped by a silyl radical,[36] therefore, branching can reach various degrees even in one QD. The existence of the branching process also implies that a solvation shell with a size non-multiple of the alkyl chain length is fully feasible. The schematic illustration of the interpretation of the branching and further layer bonding is presented in Fig. 3D. Therefore, d_{DLS} for dodecyl:SiQDs can be determined as

$$d_{DLS} = n(d_{DLS\text{-}min} + 2l_{ligand}N + l_{C\text{-}C\text{-}C}M), \qquad (2)$$

where $d_{DLS\text{-}min}$ stands for a minimal DLS-derived size and l_{ligand} denotes the chain length of the attached terminating group (1.5 nm for the dodecyl groups). N is included to describe a higher degree of oligomerization ($N = 0$ for a mono-layer coverage). The $l_{C\text{-}C\text{-}C}M$ factor addresses potential branching without *a priori* assuming two-sided symmetry, which elongates the attached alkyl by M times the length of two carbon bonds ($l_{C\text{-}C\text{-}C} = 0.25$ nm). Lastly, d_{DLS} can be influenced by potential agglomeration involving n QDs. The minimal size $d_{DLS\text{-}min}$ of a monolayer covered QD with fully extended ligands can then be written as

$$d_{DLS\text{-}min} = d + 2l_{ligand}. \qquad (3)$$

where d stands for the diameter of the QD core.

Eqn (2) and (3) help us interpret the results of the DLS measurements in Fig. 3C. Starting with the *IAS* samples, which exhibit better dispersibility, the *S*- and *M*-dodecyl:SiQDs narrow DLS-derived size distributions peak at around 9 and 12 nm, respectively. Taking into account the corresponding minimal hydrodynamical diameters ($d_{DLS\text{-}min}^{S\text{-}dodecyl} = 5.5$ nm, $d_{DLS\text{-}min}^{M\text{-}dodecyl} = 7.0$ nm), we expect monodispersion ($n = 1$) with a low degree of oligomerization and branching ($n = 1$, $N = 1$, $M \approx 2\text{-}6$). The maximum size distribution of *L*-dodecyl:SiQDs at around 19 nm ($d_{DLS\text{-}min}^{L\text{-}dodecyl} = 8.5$ nm) could imply agglomeration ($n = 2$). However, the lack of a tail in the size distribution towards $d_{DLS\text{-}min}^{L\text{-}dodecyl}$ rather signifies a higher degree of oligomerization ($n = 1$, $N = 4$). The *EL*-dodecyl:SiQDs ($d_{DLS\text{-}min}^{EL\text{-}dodecyl} = 9.3$ nm) then exhibit a bimodal size distribution with maxima at 25 and 127 nm, respectively. In line with the reasoning offered for the *L*-dodecyl:SiQD sample, we interpret the first peak as monodisperse QDs with oligomerized and likely branched surface ligands ($n = 1$, $N \approx 10$, $M > 0$). The second broader peak can then be attributed to agglomeration ($n = 15\text{-}20$), possibly induced by the bimodal distribution of the QDs before hydrosilylation (see Fig. 3C). This interpretation tentatively implies that the less reactive surface[31] of the larger QDs leads to a higher degree of oligomerization. This trend is to be expected, because a lower number of reactive sites pro-

motes reactivity on the chains. Notably, solely based on DLS, the potential aggregation due to improperly passivated partially oxidized surface cannot be ruled out, but we do not expect aggregation to be dominant in this case due to the small oxide-related signal observed in FTIR (Fig. 3A).

To study the difference between the two approaches to hydrosilylation (see section 3.2), DLS measurements of *AES*- and *IAS*-modified *M*-dodecyl:SiQDs are compared in Fig. 3C. The *AES* hydrosilylation with short air exposure leads to a broader size distribution with a maximum at around 35 nm. Thus, even the minuscule difference in surface oxidation detected by FTIR in the *AES* procedures (see Fig. 3A) increases the QDs' tendency to oxidize and form larger aggregates with partially oxidized oligomerized surface ligands ($n = 3\text{-}12$, N up to 7), as confirmed by the increased oxide-related FTIR signal in Fig. 3A.

PILR-modified SiQDs. Fig. 3E presents the comparison of the d_{DLS} of *M*-octoxy:SiQDs and *M*-etoxy:SiQDs compared to the hydrosilylated *M*-dodecyl:SiQDs, acquired using DLS. In this case, oligomerization or branching is not expected ($N = M = 0$), therefore, a simple estimate based on the DLS data can be made directly using eqn (3) with $l_{ligand}^{ethoxy} = 0.45$ nm and $l_{ligand}^{octoxy} = 1.2$ nm. However, since polar solvents promote stronger solvent—nanoparticle interactions, somewhat longer-range solvent restructuring can be expected than in non-polar solvents where the interaction with the hydrophobic surface groups is weaker. On the other hand, the degree of extension of the ligand groups clearly depends on the interplay between the polarity of the environment and the hydrophobicity/hydrophilicity of the ligands.

For *M*-etoxy:SiQDs, we obtained a narrow size distribution with a maximum at 7 nm compared to $d_{DLS\text{-}min} = 4.9$ nm. However, in this case, due to the extremely short length of the terminating groups, solvent restructuring and thus the thickness of the solvation shell detected by DLS are expected to exceed the simple chain length,[90] and therefore, a 1.5 nm solvation shell thickness derived from the difference of the HRTEM- and DLS-derived mean sizes is fully consistent with a monodispersion of ethoxy:SiQDs. For *M*-octoxy:SiQDs, we obtained a narrow size distribution, a maximum close to *M*-dodecyl:SiQDs at 15 nm ($d_{DLS\text{-}min}^{M\text{-}octoxy:SiQDs} = 6.4$ nm). Therefore, unless oligomerization occurs also in octoxy groups, *M*-octoxy:SiQDs form clusters or partially functionalized aggregates of 2–3 QDs after surface modification. In contrast, after purification and redispersion in IPA, the size distribution maximum at 52 nm points towards a higher degree of aggregation. For other sizes of the SiQDs (*L*- and *S*-), we found a similar behavior in the case of the octoxy terminated surface, leading to a narrow dispersion in the interval from 12 to 15 nm for the octoxy:SiQDs in OCT, see Fig. S5. This implies that the *S*- and *L*-octoxy:SiQDs formed agglomerates or aggregates of 4 or 2 QDs, respectively. For octoxy:SiQDs in IPA, high tendency towards aggregation was detected with distributions for *L*- and *S*-SiQDs around 100 nm. Similarly, etoxy:SiQDs were more aggregated for the *L*- and *S*-sizes with DLS dispersion maxima of 110 and 55 nm (≈ 20 QDs), respectively.

3.4. Optical properties

3.4.1. Steady-state photoluminescence and quantum yields. The H:SiQDs synthesized in our non-thermal plasma setup exhibit detectable luminescence even in the as-synthesized form, likely due to a degree of oxidation occurring before the PL measurement. With the surface termination, the PL properties are enhanced and a blue-shift of its maxima was reported, as shown in Fig. 4, where octoxy:SiQDs, ethoxy:SiQDs and hydrosilylated dodecyl:SiQDs are compared using *M*-SiQD sizes. In *M*-dodecyl:SiQDs, an immediate 6 times increase of the PL intensity followed by a slower further increase to around 9 times the original value was observed after the dodecyl surface termination (the intensities are comparable as the measurements were carried out using the same conditions), see Fig. S6. This increase was accompanied by a 100 nm blue shift, resulting in brightly red luminescent SiQDs with long-term stability, see Fig. 4C. An analogical, albeit slower trend was observed in octoxy:SiQDs, see Fig. 4A, where a blue-shift of *ca.* 90 nm was accompanied by a PL intensity increase of about 10×. As a reference, *M*-SiQDs dispersed in

OCT without any plasma treatment were also studied, see Fig. 4A, with detectable, but much lower PL intensity increase, confirming the decisive influence of the plasma treatment on a successful surface modification. A similar temporal evolution of PL occurred in ethoxy:SiQDs with a lower PL enhancement. Therefore, in all cases, we obtained surface-modified SiQDs with comparable PL spectra, see Fig. 4B, and high optical quality, see Fig. 4C. The PL properties of all the different sizes are compared in Table 2.

To quantitatively compare the optical properties, photoluminescence quantum yield (QY) measurements were carried out,[62] see Fig. 5A. The *S*-SiQD samples have the lowest PLQY overall, but the values are very similar for all the surface modifications (≈5%). The QYs of the *M* and *L*-SiQD samples vary between 10 and 20%, with the highest QY for the *M* sample achieved with dodecyl termination (20%), and the highest QY for the *L* sample achieved with octoxy termination (18%). However, the purification and IPA redispersion of octoxy: SiQDs systematically lower the QY. The QY values of the etoxy: SiQDs are consistently lower despite low agglomeration, the best QY is observed with the ethoxy surface ligand in *M*-etoxy:
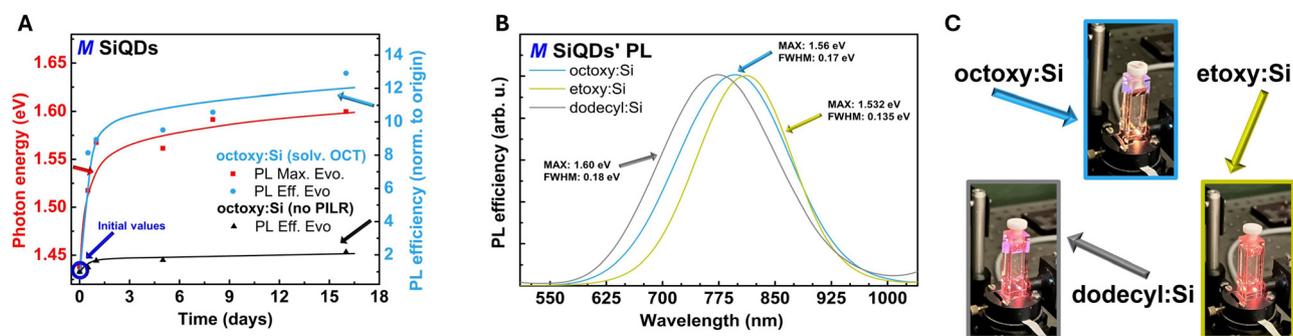

Fig. 4 Optical properties of the PILR-modified SiQDs: (A) long-term evolution of the PL properties of *M*-octoxy:SiQDs and (B) a comparison of the PILR-OCT processed SiQDs with those simply dispersed in OCT. (C) Comparison of the PL spectra of *M*-dodecyl:SiQDs, *M*-etoxy:SiQDs and *M*-octoxy:SiQDs accompanied by photos of PL of selected *M*-SiQDs (cw excitation at 325 nm).
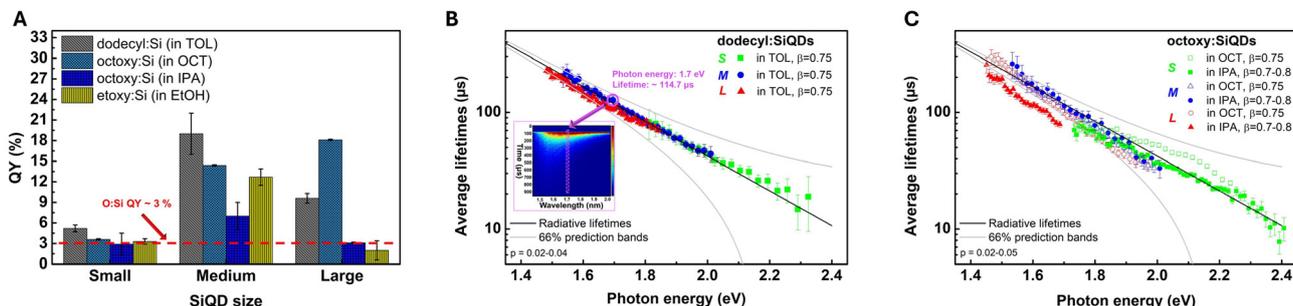

Fig. 5 Photoluminescence properties of the studied SiQDs. (A) Measured photoluminescence quantum yield for different sample sizes and types of surface modifications. (B and C) Average photoluminescence lifetimes (data points) deduced from single stretched-exponential fits are compared with the values of fully radiative lifetimes[60] (black curves and gray bordered area) in SiQDs for the dodecyl (B) and octoxy (C) surface modification (see the text for details). The black curve marks the fully radiative lifetimes, the gray bordered areas are 66% prediction bands. The β parameters of the stretched-exponential decays are listed in the legends, fit ambiguity coefficients[60] p are listed in each panel. Inset in (B) (photon-map) shows that one data point refers to the average lifetime for the selected wavelength.

SiQDs (12%). The overall trend of QY values peaking for SiQD samples emitting at around 850 nm is analogous to other publications.[91–93]

3.4.2. Photoluminescence dynamics and dark QDs.
Further insight into the photoluminescence properties of the studied SiQDs can be gained by characterizing their PL decays. Unlike in other studies, our dedicated analysis[60,63] allows us to quantify the emission-wavelength-resolved radiative lifetimes, a fundamental optical characteristic of an emitting sample. (Please note that radiative lifetimes are sometimes reported incorrectly[94,95] using an assumption that all the QDs in the studied ensemble have the same QY.[60]) In contrast to our approach, many studies lack the spectral resolution or report solely the fitted lifetime values without the necessary analysis,[35,41] which is crucial if a physically meaningful interpretation is to be obtained because of the strong dependence of PL lifetimes on the emission photon energy in SiQDs.[60] Moreover, when the ensemble QY is taken into account, we can also calculate the fraction of dark QDs, which are almost never reported. For a comparison of the difference in the parameters obtained from spectrally resolved and spectrally integrated PL, as well as the difference between the types of lifetimes used for the analysis, see Table 2 and Fig. 5B, C.

To carry out the analysis, a set of emission-photon-wavelength dependent PL decays was collected for each sample and these decays were subsequently characterized[63] using the corresponding average lifetimes τ (see eqn (1) in section 2.10), which allow for a meaningful comparison among independent measurements.[60]

In dodecyl:SiQDs, the PL decays were well-characterized using a single stretched-exponential curve (see section 2.10). As follows from the reasoning explained in ref. 60, the obtained average photoluminescence lifetimes in dodecyl:SiQDs are very close to the fully radiative values, see Fig. 5B, implying that the emitting dodecyl:SiQDs have internal QY[60] $\eta_I^{dodecyl}$ close to 1. The emitting subset of SiQDs will be referred to as "bright". The decrease of the measured ensemble-averaged QY η from the ideal 100% values as seen in Fig. 5A is then caused by the presence of non-emitting, or "dark" QDs, whose fraction $D = \dfrac{N_{dark}}{N_{bright}}$ can be easily estimated as[60]

$$D = \frac{\eta_I - \eta}{\eta}. \tag{4}$$

The estimated ratios of dark-to-bright dodecyl:SiQDs, ranging between 4 and 20 : 1, are listed in Table 2.

In octoxy:SiQDs, PL decays differed for samples prior to and after the purification procedure. The PL decays of octoxy:SiQDs stored in octanol were practically identical to those of dodecyl:SiQDs, including the fully radiative values and the consequent close-to-unity η_I. In contrast, the PL decays of purified octoxy:SiQDs in isopropanol consist of two components, as a much faster, resolution-limited component appeared in addition to the traditional long-lived one, see Fig. S7C. The average lifetimes τ calculated solely for the long-lived component (Fig. 5C) again well correspond to the fully radiative

values, with the exception of purified *L*-octoxy:SiQDs, where the measured τ is systematically shorter. Based on the methodology introduced in ref. 60 (see eqn (7) therein), we can easily calculate, using the data from Fig. 5C, the scaling factor C of the experimental average lifetimes $\tau^{L-octoxy:SiQDs}$ to the ideal fully radiative ones τ_{rad} as $C = \tau^{L-octoxy:SiQDs}/\tau_{rad} = (0.866 \pm 0.006)$. This scaling factor immediately yields the estimated internal QY of $\eta_I^{L-octoxy:SiQDs} = C \approx 0.85$. Thus, unlike the remaining samples, the purified *L*-octoxy:SiQDs emitting the long-lived PL are not ideally bright with a clear presence of a long-lived non-radiative channel.

Moreover, in addition to the long-lived PL channel, all the purified octoxy:SiQD samples exhibit an additional faster component with only a weak emission-photon-energy dependence, see Fig. S7D. The most straightforward interpretation of this faster component is emission strongly damped by relatively fast non-radiative processes, resulting in the weak emission–photon-energy dependence. Therefore, this component can be tentatively ascribed to "gray" QDs, most likely originating from the agglomeration of QDs observed in IPA. The complex makeup of these samples, containing "bright", "gray" and "dark" sub-populations of QDs, prevents us from applying the simple methodology[60] for the estimation of the ratios of the individual sub-populations. Nevertheless, the proposed interpretation is fully consistent with the trends observed in the measured ensemble-averaged QY values in Fig. 5A, where (i) a ≈2× decrease in QY is observed between non-purified and purified samples, due to the presence of "gray" QDs in the latter, and (ii) an additional QY decrease is detected between the purified *M*- and *L*-octoxy:SiQDs as a result of the long-lived non-radiative channel in the *L* sample. This can be correlated with the higher degree of agglomeration for the *L*-octoxy:SiQDs in IPA, *ca.* 100 nm (see Fig. S5) and a lower degree of agglomeration in *M*-octoxy:SiQDs in IPA (*ca.* 52 nm, see Fig. 2D).

Additionally a fast yellow PL component appears in octoxy:SiQDs, especially in the *M*-octoxy:SiQD sample, see Fig. S8A. We note that this component persists in the sample even after the centrifugation-based purification procedure. We verified that it is not present in the reference sample of plasma-initiated octanol without SiQDs, see Fig. S8B. Without an in-depth discussion, we hypothesize that the PILR treatment of octanol-dispersed SiQDs might produce luminescent carbon dots, which are known to arise from a solvothermal treatment.[25,96]

The PL decays of the ethoxy:SiQDs were then similar to the purified octoxy:SiQDs in IPA, being a combination of a resolution-limited single exponential corresponding to "gray" SiQDs and a long-lived stretched-exponential function with measured lifetimes well matching the fully radiative ones, representing bright SiQDs (see Fig. S9). The contribution of "gray" SiQDs is pronounced in *S*-ethoxy:SiQDs and relatively marginal in *M*- and *L*-ethoxy:SiQDs, see Fig. S10. Because of the marginal contribution of the "gray" QDs, we believe that the calculation of the ratio of dark SiQDs using eqn (4) is still a very reasonable estimate for both the *M*- and *L*-ethoxy:SiQDs, see Table 2, while for *S*-etoxy:SiQDs, it can serve only as an upper limit.

Overall, our results confirm that the main radiative pathway in carbon-linked hydrosilylated and alkoxylated SiQDs is mostly the same, including the same radiative lifetimes of the recombination process. The same conclusion of mostly similar excited state dynamics in these two systems has recently been published elsewhere including extensive transient-absorption data.[52] Consequently, the main difference seems to lie in dark QDs, which makes them an important problem to focus on.

Dark SiQDs have so far been systematically studied only in oxide-passivated matrix-embedded samples,[93,97] where the application of the Purcell effect to directly determine the internal quantum yield is possible.[60,93] Limpens *et al.*[97] deduced the fraction of dark QDs D using an approach similar to ours, in particular from a comparison of literature-based radiative rates with measured lifetimes. Their relatively crude analysis of PL decays disregarding the clearly present faster initial term very likely contributes to a larger margin of error, but their deduced D values are close to ours, ranging between 5 and 2.2 before and after a passivation treatment for samples nominally closest to our *M*-SiQDs. Valenta *et al.*[93] directly measured the internal quantum yield using the Purcell effect and their reported emission-wavelength-resolved D's range between 0.25 and 20 with the lowest values at an emission wavelength of around 860 nm and a systematic rise towards shorter emission wavelengths. Thus, the dark-to-bright QD ratio D in their samples is smaller than in the ones studied here, but at a cost of producing their SiQDs by fabricating a complex multilayer structure by a two-step annealing process.

Our optical studies allow us to directly compare the ratio of dark-to-bright QDs and the number of QDs in agglomerates and, in this way, to assess the influence of agglomeration on QY, see Fig. 6. The trend of PL quenching with increasing agglomeration independent of size or type of surface passivation is clearly observable. Monodispersed SiQDs showed the lowest number of dark QDs, reaching the maximal QY for our

samples. Agglomeration-induced PL quenching is further supported by the difference between *IAS* and *AES* hydrosilylation approaches, where in the *AES*-modified SiQDs the agglomeration was higher, and their PL performance was worse. The same phenomenon was also encountered in octoxy:SiQDs. After redispersion in IPA, the agglomeration was higher and the PLQY was significantly lower. As for the smallest *S*-SiQDs, they also showed a similar trend of PL quenching with higher agglomeration, with a somewhat weaker dependency of the dark QD ratio on the agglomeration, but with consistently the worst PL performance (the best QY for the monoQDs around 5%). The trend of lower QY at the smallest SiQD sizes agrees with previous observations.[36,57]

However, even without agglomeration, we are currently unable to reach QYs higher than 20% using both hydrosilylation and PILR, implying that an additional effect is the limiting factor here. Therefore, to reach higher PL QYs and lower the number of dark SiQDs, two approaches are possible: (i) tuning the as-synthesized surface with respect to our previous work[31] and (ii) selecting the right ligand and termination method for the given surface and size of the QDs.

4. Conclusion

In this article, we focus on the synthesis and surface modification of luminescent SiQDs. Using synthesis in non-thermal plasma, we are able to quickly synthesize crystalline SiQDs of desired sizes ranging from 6 down to 2.4 nm, which represents one of the smallest sizes reported for plasma synthesis, with a narrow and symmetric size distribution and reactive surface. In the synthesis step, we employ a home-built 3D printed flow-box for sample extraction, which simplifies future development of the apparatus and combines versatility and scalability while keeping the costs low. Subsequently, we also simplified the surface modification process by omitting the freeze–pump–thaw cycles in the conventional thermal hydrosilylation with 1-dodecene and by advancing the scalable and cheap plasma-induced in-liquid reactions (PILRs) for organic capping ligands of different lengths and polarities. The PILR-modified SiQDs are mainly characterized by a mixed capping of oxide and the semi-polar octoxy- and polar ethoxy-groups, respectively. Both hydrosilylated and PILR-modified SiQDs were brightly luminescent (PLQY reaching up to 20%) with comparable optical performance. Both methods also report good dispersibility, achieving monodispersed SiQDs in specific environments. Detailed discussion of the determination of the distribution of sizes including the difference between the XRD- and HRTEM-derived sizes and the oligomerization of surface ligands and agglomeration is provided. Using a dedicated optical characterization method, we show that we can produce ideally bright SiQDs with close-to-unity internal QY, implying that dark QDs, present in the range of $4:1$–$30:1$ with respect to the bright QDs, cause the measured lower-than-unity external QYs. By comparing the fundamental sample properties of the number of dark QDs with the
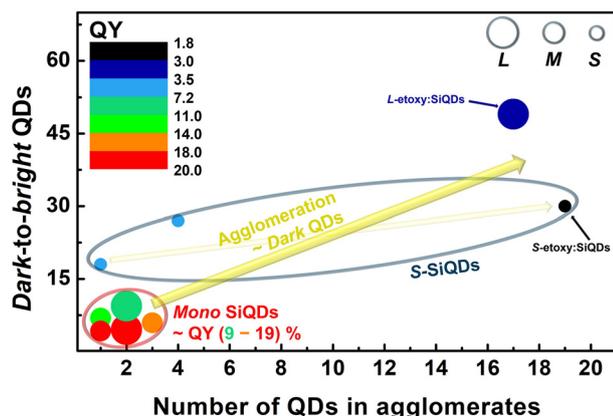

Fig. 6 Schematic summary of the dependency of the dark-to-bright QD ratio on the agglomeration of SiQDs. Strong agglomeration-induced quenching occurs in *L*- and *M*-SiQDs. A weaker trend is observed for *S*-SiQDs (2.4 nm) due to their size and the initially higher number of dark QDs.

number of QDs in an agglomerate, we observe a clear correlation between agglomeration and PL quenching *via* dark QDs. Thus, our study provides essential guidelines regarding the synthesis, surface modification, and optical and dispersive properties of SiQDs. Our results are of particular importance for developing up-scalable and non-demanding synthesis and surface modification processes for future optical and optoelectronic applications, as well as for understanding the fundamental properties of SiQDs and their colloidal dispersions.

Author contributions

F. M. built and designed the synthesis and PILR setups, suggested the capping molecules, carried out the synthesis of samples, all hydrosilylation and PILR experiments, FTIR characterization, contributed to the QY and time-resolved measurements and significantly participated in outlining, drafting and revising the manuscript. P. G. carried out the DLS measurements, suggested and contributed to the idea of the PILR method and helped building the non-thermal plasma synthesis setup. J. K. participated in the building of the PILR setup and contributed to setting of the PILR methodology, mainly to setting the plasma parameters. M. D. carried out and interpreted the XRD measurements. A. M. carried out the HRTEM measurements and helped with their interpretation and analysis. T. P. built the setup for measurement of QY and helped with the interpretation of time-resolved measurements. J. B. gave insight into plasma parameters and worked as a technical support regarding plasma setting. K. K. supervised the project, contributed to the hydrosilylation process, mainly the purification process, carried out the time-resolved PL measurements and their interpretation, helped with the QY measurements and significantly participated in outlining, drafting and revising the manuscript.

Conflicts of interest

There are no conflicts to declare.

Data availability

The data supporting this article have been included as part of the supplementary information (SI). Supplementary information is available. See DOI: https://doi.org/10.1039/d5nr03184b. In the Supplementary Information additional photographs of the dispersions of SiQDs, HRTEM images for EL-, M- and S-SiQDs, comparison of the distrubutions determined using XRD and HRTEM and further DLS measurements info are presented. In the Supplementary Information further time-resolved and steady-state luminescence properties are listed. All of these data are referenced in the main text.

Other measured data and software used for the evaluation of the QY and decays can be obtained from the corresponding author on reasonable request.

Acknowledgements

References

1 M. V. Kovalenko, L. Manna, A. Cabot, Z. Hens, D. V. Talapin, C. R. Kagan, V. I. Klimov, A. L. Rogach, P. Reiss, D. J. Milliron, P. Guyot-Sionnnest, G. Konstantatos, W. J. Parak, T. Hyeon, B. A. Korgel, C. B. Murray and W. Heiss, *ACS Nano*, 2015, **9**, 1012–1057.

2 S. Milliken, A. N. Thiessen, I. T. Cheong, K. M. O'Connor, Z. Li, R. W. Hooper, C. J. T. Robidillo and J. G. C. Veinot, *Nanoscale*, 2021, **13**, 16379–16404.

3 D. Beri, *Mater. Adv.*, 2023, **4**, 3380–3398.

4 S. K. E. Hill, R. Connell, J. Held, C. Peterson, L. Francis, M. A. Hillmyer, V. E. Ferry and U. Kortshagen, *ACS Appl. Mater. Interfaces*, 2020, **12**, 4572–4578.

5 R. Mazzaro, A. Gradone, S. Angeloni, G. Morselli, P. G. Cozzi, F. Romano, A. Vomiero and P. Ceroni, *ACS Photonics*, 2019, **6**, 2303–2311.

6 J. Huang, J. Zhou, E. Jungstedt, A. Samanta, J. Linnros, L. A. Berglund and I. Sychugov, *ACS Photonics*, 2022, **9**, 2499–2509.

7 X. Liu, S. Zhao, W. Gu, Y. Zhang, X. Quo, Z. Ni, X. Pi and D. Yang, *ACS Appl. Mater. Interfaces*, 2018, **10**, 5959–5966.

8 B. Ghosh, H. Yamada, S. Chinnathambi, I. N. G. Özbilgin and N. Shirahata, *J. Phys. Chem. Lett.*, 2018, **9**, 5400–5407.

9 C. M. Gonzalez, M. Iqbal, M. Dasog, D. G. Piercey, R. Lockwood, T. M. Klapotke and J. G. C. Veinot, *Nanoscale*, 2014, **6**, 2608–2612.

10 S. Terada, H. Ueda, T. Ono and K.-i. Saitow, *ACS Sustainable Chem. Eng.*, 2022, **10**, 1765–1776.

11 D. Yang, Z. Cui, Z. Wen, Z. Piao, H. He, X. Wei, L. Wang, S. Mei, W. Zhang and R. Guo, *ACS Mater. Lett.*, 2023, **5**, 985–1008.

12 K. M. Neethu, S. Karmakar, B. Sahoo, N. Mishrra and P. Moitra, *Small*, 2025, **21**, 2407353.

13 H. Kim, M. Seo, M.-H. Park and J. Cho, *Angew. Chem., Int. Ed.*, 2010, **49**, 2146–2149.

14 T. Mizutani, H. Ohta, T. Ueda, T. Kashiwagi, T. Fukuda, T. Shiobara and K.-i. Saitow, *ACS Sustainable Chem. Eng.*, 2023, **11**, 11769–11780.

15 L. Mangolini, E. Thimsen and U. Kortshagen, *Nano Lett.*, 2005, **5**, 655–659.

16 L. Mangolini, D. Jurbergs, E. Rogojina and U. Kortshagen, *J. Lumin.*, 2006, **121**, 327–334.

17 U. R. Kortshagen, R. M. Sankaran, R. N. Pereira, S. L. Girshick, J. J. Wu and E. S. Aydil, *Chem. Rev.*, 2016, **116**, 11061–11127.

18 S. Askari, I. Levchenko, K. Ostrikov, P. Maguire and D. Mariotti, *Appl. Phys. Lett.*, 2014, **104**, 163103.

19 B. Barwe, F. Riedel, O. Cibulka, I. Pelant and J. Benedikt, *J. Phys. D: Appl. Phys.*, 2015, **48**, 314001.

20 T. A. Pringle, K. I. Hunter, A. Brumberg, K. J. Anderson, J. A. Fagan, S. A. Thomas, R. J. Petersen, M. Sefannaser, Y. Han, S. L. Brown, D. S. Kilin, R. D. Schaller, U. R. Kortshagen, P. R. Boudjouk and E. K. Hobbie, *ACS Nano*, 2020, **14**, 3858–3867.

21 C. M. Hessel, E. J. Henderson and J. G. C. Veinot, *Chem. Mater.*, 2006, **18**, 6139–6146.

22 J. Zhou, J. Huang, H. Chen, A. Samanta, J. Linnros, Z. Yang and I. Sychugov, *J. Phys. Chem. Lett.*, 2021, **12**, 8909–8916.

23 J. Valenta, M. Greben, S. Gutsch, D. Hiller and M. Zacharias, *J. Appl. Phys.*, 2017, **122**, 144303.

24 B. F. P. McVey and R. D. Tilley, *Acc. Chem. Res.*, 2014, **47**, 3045–3051.

25 J. B. Essner, J. A. Kist, L. Polo-Parada and G. A. Baker, *Chem. Mater.*, 2018, **30**, 1878–1887.

26 B. V. Oliinyk, D. Korytko, V. Lysenko and S. Alekseev, *Chem. Mater.*, 2019, **31**, 7167–7172.

27 J. Wilbrink, C.-C. Huang, K. Dohnalova and J. M. J. Paulusse, *Faraday Discuss.*, 2020, **222**, 149–165.

28 R. J. Clark, M. Aghajamali, C. M. Gonzalez, L. Hadidi, M. A. Islam, M. Javadi, M. H. Mobarok, T. K. Purkait, C. J. T. Robidillo, R. Sinelnikov, A. N. Thiessen, J. Washington, H. Yu and J. G. C. Veinot, *Chem. Mater.*, 2017, **29**, 80–89.

29 M. Dworschak, N. Kohlmann, F. Matějka, P. Galář, L. Kienle, J. Schäfer and J. Benedikt, *Plasma Processes Polym.*, 2023, **20**, 2200129.

30 L. Mangolini and U. Kortshagen, *Adv. Mater.*, 2007, **19**, 2513–2519.

31 P. Galář, J. Kopenec, R. Král, F. Matějka, P. Zemenová, M. Dopita, P. Hapala, D. König, P. Vrbka and K. Kůsová, *ACS Nano*, 2025, **19**, 2196–2212.

32 F. A. Reboredo and G. Galli, *J. Phys. Chem. B*, 2005, **109**, 1072–1078.

33 J. M. Buriak, *Chem. Rev.*, 2002, **102**, 1271–1308.

34 F. A. Reboredo, E. Schwegler and G. Galli, *J. Am. Chem. Soc.*, 2003, **125**, 15243–15249.

35 Z. Yang, C. M. Gonzalez, T. K. Purkait, M. Iqbal, A. Meldrum and J. G. C. Veinot, *Langmuir*, 2015, **31**, 10540–10548.

36 L. M. Wheeler, N. C. Anderson, P. K. B. Palomaki, J. L. Blackburn, J. C. Johnson and N. R. Neale, *Chem. Mater.*, 2015, **27**, 6869–6878.

37 J. A. Kelly, A. M. Shukaliak, M. D. Fleischauer and J. G. C. Veinot, *J. Am. Chem. Soc.*, 2011, **133**, 9564–9571.

38 D. Beri, D. Busko, A. Mazilkin, I. A. Howard, B. S. Richards and A. Turshatov, *RSC Adv.*, 2018, **8**, 9979–9984.

39 Y. Yu and B. A. Korgel, *Langmuir*, 2015, **31**, 6532–6537.

40 R. J. Clark, M. Aghajamali, C. M. Gonzalez, L. Hadidi, M. A. Islam, M. Javadi, M. H. Mobarok, T. K. Purkait, C. J. T. Robidillo, R. Sinelnikov, A. N. Thiessen, J. Washington, H. Yu and J. G. C. Veinot, *Chem. Mater.*, 2017, **29**, 80–89.

41 C. J. T. Robidillo, M. A. Islam, M. Aghajamali, A. Faramus, R. Sinelnikov, X. Zhang, J. Boekhoven and J. G. C. Veinot, *Langmuir*, 2018, **34**, 6556–6569.

42 J. J. Wu, V. S. S. K. Kondeti, P. J. Bruggeman and U. R. Kortshagen, *J. Phys. D: Appl. Phys.*, 2016, **49**, 08LT02.

43 P. J. Bruggeman, M. J. Kushner, B. R. Locke, J. G. E. Gardeniers, W. G. Graham, D. B. Graves, R. C. H. M. Hofman-Caris, D. Maric, J. P. Reid, E. Ceriani, D. F. Rivas, J. E. Foster, S. C. Garrick, Y. Gorbanev, S. Hamaguchi, F. Iza, H. Jablonowski, E. Klimova, J. Kolb, F. Krcma, P. Lukes, Z. Machala, I. Marinov, D. Mariotti, S. M. Thagard, D. Minakata, E. C. Neyts, J. Pawlat, Z. L. Petrovic, R. Pflieger, S. Reuter, D. C. Schram, S. Schrater, M. Shiraiwa, B. Tarabova, P. A. Tsai, J. R. R. Verlet, T. von Woedtke, K. R. Wilson, K. Yasui and G. Zvereva, *Plasma Sour. Sci. Technol.*, 2016, **25**, 053002.

44 V. Švrček, D. Mariotti and M. Kondo, *Appl. Phys. Lett.*, 2010, **97**, 161502.

45 D. Mariotti, V. Švrček, J. W. J. Hamilton, M. Schmidt and M. Kondo, *Adv. Funct. Mater.*, 2012, **22**, 954–964.

46 D. Mariotti, S. Mitra and V. Švrček, *Nanoscale*, 2013, **5**, 1385–1398.

47 P. Galář, A. Fučiková, K. Newell, T. Popelář, I. Matulková, J. Valenta, V. Scholtz and K. Kůsová, *Green Chem.*, 2021, **23**, 898–911.

48 F. Matějka, P. Galář, J. Khun, V. Scholtz and K. Kůsová, *Phys. Scr.*, 2022, **98**, 045619.

49 S. Askari, M. Macias-Montero, T. Velusamy, P. Maguire, V. Svrcek and D. Mariotti, *J. Phys. D: Appl. Phys.*, 2015, **48**, 314002.

50 J. P. Bell, J. E. Cloud, J. Cheng, C. Ngo, S. Kodambaka, A. Sellinger, S. K. Ratanathanawongs Williams and Y. Yang, *RSC Adv.*, 2014, **4**, 51105–51110.

51 Y. Zhai, M. Dasog, R. B. Snitynsky, T. K. Purkait, M. Aghajamali, A. H. Hahn, C. B. Sturdy, T. L. Lowary and J. G. C. Veinot, *J. Mater. Chem. B*, 2014, **2**, 8427–8433.

52 M. Lai, L. Wei, Y.-H. Huang, X.-D. Wang and Z. Yang, *ACS Photonics*, 2024, **11**, 2439–2449.

53 K.-i. Saitow, *Bull. Chem. Soc. Jpn.*, 2024, **97**, uoad002.

54 K. Kůsová, *Phys. Status Solidi A*, 2018, **215**, 1700718.

55 T. Popelář, F. Matějka, J. Kopenec, G. Morselli, P. Ceroni and K. Kůsová, *Nanoscale Adv.*, 2024, **6**, 2644–2655.

56 M. Dasog, G. B. D. los Reyes, L. V. Titova, F. A. Hegmann and J. G. C. Veinot, *ACS Nano*, 2014, **8**, 9636–9648.

57 Z. Li and U. R. Kortshagen, *Chem. Mater.*, 2019, **31**, 8451–8458.

58 R. Mazzaro, A. Gradone, S. Angeloni, G. Morselli, P. G. Cozzi, F. Romano, A. Vomiero and P. Ceroni, *ACS Photonics*, 2019, **6**, 2303–2311.

59 D. Jurbergs, E. Rogojina, L. Mangolini and U. Kortshagen, *Appl. Phys. Lett.*, 2006, **88**, 233116–233118.

60 T. Popelář, P. Galář, F. Matějka, G. Morsellli, P. Ceroni and K. Kůsová, *J. Phys. Chem. C*, 2023, **127**, 20426–20437.

61 Z. Matěj, A. Kadlecová, M. Janeček, L. Matějová, M. Dopita and R. Kužel, *Powder Diffr.*, 2014, **29**, S35–S41.

62 K. Kůsová, T. Popelář, F. Matějka and M. Vašíček, *Adv. Quantum Technol.*, 2025, **8**, e00228.

63 K. Kůsová and T. Popelář, *J. Appl. Phys.*, 2019, **125**, 193103.

64 U. Kortshagen, *J. Phys. D: Appl. Phys.*, 2009, **42**, 113001.

65 C. Tsai, G. Anderson and R. Thompson, *J. Non-Cryst. Solids*, 1991, **137–138**, 673–676.

66 A. N. Thiessen, M. Ha, R. W. Hooper, H. Yu, A. O. Oliynyk, J. G. Veinot and V. K. Michaelis, *Chem. Mater.*, 2019, **31**, 678–688.

67 A. N. Thiessen, L. Zhang, A. O. Oliynyk, H. Yu, K. M. O'Connor, A. Meldrum and J. G. C. Veinot, *Chem. Mater.*, 2020, **32**, 6838–6846.

68 H. Borchert, E. V. Shevchenko, A. Robert, I. Mekis, A. Kornowski, G. Grübel and H. Weller, *Langmuir*, 2005, **21**, 1931–1936.

69 L. Fekete, K. Kůsová, V. Petrák and I. Kratochvílová, *J. Nanopart. Res.*, 2012, **14**, 1062.

70 Z. Matěj, A. Kadlecová, M. Janeček, L. Matějová, M. Dopita and R. Kužel, *Powder Diffr.*, 2014, **29**, S35–S41.

71 C. F. Holder and R. E. Schaak, *ACS Nano*, 2019, **13**, 7359–7365.

72 B. N. Jariwala, N. J. Kramer, M. C. Petcu, D. C. Bobela, M. C. M. v. d. Sanden, P. Stradins, C. V. Ciobanu and S. Agarwal, *J. Phys. Chem. C*, 2011, **115**, 20375–20379.

73 D. C. Marra, E. A. Edelberg, R. L. Naone and E. S. Aydil, *J. Vac. Sci. Technol., A*, 1998, **16**, 3199–3210.

74 J. Holm and J. T. Roberts, *Langmuir*, 2007, **23**, 11217–11224.

75 G. M. Carroll, R. Limpens and N. R. Neale, *Nano Lett.*, 2018, **18**, 3118–3124.

76 M. P. Stewart and J. M. Buriak, *Comments Inorg. Chem.*, 2002, **23**, 179–203.

77 Y. Ogata, H. Niki, T. Sakka and M. Iwasaki, *J. Electrochem. Soc.*, 1995, **142**, 195.

78 C. T. Kirk, *Phys. Rev. B: Condens. Matter Mater. Phys.*, 1988, **38**, 1255–1273.

79 S. Gardelis, A. G. Nassiopoulou, M. Mahdouani, R. Bourguiga and S. Jaziri, *Phys. E*, 2009, **41**, 986–989.

80 D. B. Mawhinney, J. A. Glass Jr. and J. T. Yates Jr., *J. Phys. Chem. B*, 1997, **101**, 1202–1206.

81 K. Kůsová, O. Cibulka, K. Dohnalová, I. Pelant, J. Valenta, A. Fučíková, K. Žídek, J. Lang, J. Englich, P. Matějka, P. Štěpánek and S. Bakardjieva, *ACS Nano*, 2010, **4**, 4495–4504.

82 D. A. Long, *J. Raman Spectrosc.*, 2004, **35**, 905–905.

83 J. E. Bateman, R. D. Eagling, B. R. Horrock and A. Houlton, *J. Phys. Chem. B*, 2000, **104**, 5557–5565.

84 Y. Li, J. Liu, F. Zhao, K. Song, L. Nie, D. Liu and X. Lu, *High Voltage*, 2023, **8**, 833–840.

85 M. A. Almubarak and A. Wood, *J. Electrochem. Soc.*, 1977, **124**, 1356.

86 S. K. Filippov, R. Khusnutdinov, A. Murmiliuk, W. Inam, L. Y. Zakharova, H. Zhang and V. V. Khutoryanskiy, *Mater. Horiz.*, 2023, **10**, 5354–5370.

87 Z. Yang, M. Iqbal, A. R. Dobbie and J. G. C. Veinot, *J. Am. Chem. Soc.*, 2013, **135**, 17595–17601.

88 M. P. Hanrahan, Y. Chen, R. Blome-Fernández, J. L. Stein, G. F. Pach, M. A. S. Adamson, N. R. Neale, B. M. Cossairt, J. Vela and A. J. Rossini, *J. Am. Chem. Soc.*, 2019, **141**, 15532–15546.

89 S. Leekumjorn, S. Gullapalli and M. Wong, *J. Phys. Chem. B*, 2012, **116**, 13063–13070.

90 M. Zobel, R. B. Neder and S. A. J. Kimber, *Science*, 2015, **347**, 292–294.

91 K. Dohnalová, T. Gregorkiewicz and K. Kůsová, *J. Phys.: Condens. Matter*, 2014, **26**, 173201.

92 M. L. Mastronardi, F. Maier-Flaig, D. Faulkner, E. J. Henderson, C. Kübel, U. Lemmer and G. A. Ozin, *Nano Lett.*, 2012, **12**, 337–342.

93 J. Valenta, M. Greben, S. A. Dyakov, N. A. Gippius, D. Hiller, S. Gutsch and M. Zacharias, *Sci. Rep.*, 2019, **9**, 11214.

94 X. Liu, Y. Zhang, T. Yu, X. Qiao, R. Gresback, X. Pi and D. Yang, *Part. Part. Syst. Charact.*, 2016, **33**, 44–52.

95 F. Maier-Flaig, E. J. Henderson, S. Valouch, S. Klinkhammer, C. Kübel, G. A. Ozin and U. Lemmer, *Chem. Phys.*, 2012, **405**, 175–180.

96 Y. Wang and A. Hu, *J. Mater. Chem. C*, 2014, **2**, 6921–6939.

97 R. Limpens and T. Gregorkiewicz, *J. Appl. Phys.*, 2013, **114**, 074304.